arXiv:2201.05102v1 [stat.AP] 13 Jan 2022

Space-time extremes of severe US thunderstorm environments

Jonathan Koh*
and
Erwan Koch
and
Anthony C. Davison

Institute of Mathematics,
Ecole Polytechnique Fédérale de Lausanne (EPFL),
1015 Lausanne, Switzerland

January 14, 2022

Abstract

Severe thunderstorms cause substantial economic and human losses in the United States (US). Simultaneous high values of convective available potential energy (CAPE) and storm relative helicity (SRH) are favorable to severe weather, and both they and the composite variable PROD $= \sqrt{\text{CAPE}} \times \text{SRH}$ can be used as indicators of severe thunderstorm activity. Their extremal spatial dependence exhibits temporal non-stationarity due to seasonality and large-scale atmospheric signals such as El Niño-Southern Oscillation (ENSO). In order to investigate this, we introduce a space-time model based on a max-stable, Brown–Resnick, field whose range depends on ENSO and on time through a tensor product spline. We also propose a max-stability test based on empirical likelihood and the bootstrap. The marginal and dependence parameters must be estimated separately owing to the complexity of the model, and we develop a bootstrap-based model selection criterion that accounts for the marginal uncertainty when choosing the dependence model. In the case study, the out-sample performance of our model is good. We find that extremes of PROD, CAPE and SRH are more localized in summer and less localized during El Niño events, and give meteorological interpretations of these phenomena.

Keywords: Bootstrap; Brown–Resnick random field; El Niño-Southern Oscillation; Model selection; Non-stationary extremal dependence; Severe thunderstorm environment.

*The authors gratefully acknowledge the Swiss National Science Foundation (project 200021_178824) for funding, and Daniela Domeisen for meteorological help.

1 Introduction

Severe thunderstorms cause a substantial fraction of the economic and human losses due to natural disasters in the United States (US), such as those due to the tornadoes experienced across six states on 10–11 December 2021, so it is imperative to have a good understanding of their origins. A severe US thunderstorm is defined as one that produces tornadoes, hailstones over one inch (2.54 cm) in diameter, or wind gusts in excess of 50 kts (1 kt corresponds to approximately 0.51 m s^{-1}). Supercells, which are thunderstorms with a deep and persistent rotating updraft, are responsible for many severe thunderstorm reports (79% of tornadoes, for example, according to Trapp et al., 2005), even though only about 10% of thunderstorms are supercells (Doswell III, 2015).

The available thunderstorm data record is compromised by issues such as observational bias that complicate its use for modelling (Verbout et al., 2006; Allen and Tippett, 2015; Edwards et al., 2018), so it is worthwhile to consider meteorological environments that are conducive to severe thunderstorms. Such storms, especially supercell storms, are more probable in the presence of elevated values of convective available potential energy (CAPE) and of certain measures of vertical wind shear (e.g., Brooks et al., 2003; Brooks, 2013) such as storm relative helicity (SRH), which have been used by weather forecasters and climatologists for more than two decades. High values of the combined variable PROD = $\sqrt{\text{CAPE}} \times \text{SRH}$ are favorable to severe thunderstorms, and PROD has been used as a proxy of severe thunderstorm activity (e.g., by Tippett et al., 2016; Koch et al., 2021); see for example Brooks et al. (2003, Equation (1)) and Koch et al. (2021, Section 1) for justification for this. In addition to the absence of observational bias, an advantage of using thunderstorm environments as a proxy for thunderstorm reports is that their reanalysis values are available at high and regular spatio-temporal resolution (typically 1° longitude and 1° latitude every hour or three hours), which allows techniques from extreme-value theory and geostatistics to be applied. Among papers that have studied the temporal evolution of the extremes of a quantity similar to PROD over part of the

contiguous US are Gilleland et al. (2013), who applied the conditional extreme-value model of Heffernan and Tawn (2004) to WS $\times W_{\max}$, where WS is a measure of wind shear and $W_{\max} = \sqrt{2 \times \text{CAPE}}$, Mannshardt and Gilleland (2013), who fitted the generalized extreme-value (GEV) distribution to the annual maxima of WS $\times W_{\max}$, and Heaton et al. (2011), who considered, for the same variable, a Bayesian hierarchical extreme-value model based on a Poisson point process. Other studies have investigated the link between ENSO and seasonal or monthly means of environments during winter and spring in the US (Allen et al., 2015; Lepore et al., 2017), or between ENSO and monthly maxima of environments such as PROD, CAPE and SRH (Koch et al., 2021). Gilleland et al. (2013) studied the time evolution of spatial patterns of rather extreme events, but did not incorporate the effect of time in their model or consider pointwise maxima. The other papers mentioned above focus on the influence of time or ENSO at the marginal level (grid point by grid point) only, and, to the best of our knowledge, no article has yet considered the potential influence of these variables or more general time-varying covariates on the spatial dependence of maxima. This issue is nevertheless prominent for risk analysis, and both data and physical arguments suggest that large-scale signals such as ENSO, or seasonality, may affect extremal spatial dependence, for instance through the characteristic dimension of individual extreme events.

In this paper we address this question by using a space-time model that consists, at each time point, of a max-stable field whose dependence structure can evolve as a function of large-scale atmospheric signals or seasonal effects. We use reanalysis data from the North American Regional Reanalysis (NARR), and focus on PROD, CAPE and SRH from 1979 to 2015 over a large rectangle of the contiguous US that contains Tornado Alley, its riskiest region. Max-stable fields (e.g., de Haan, 1984; de Haan and Ferreira, 2006; Davison et al., 2012) provide a natural extension of multivariate extreme-value distributions to the infinite-dimensional setting. They are well-suited to model spatial extremes, as they arise as the only possible non-degenerate limiting random fields of appropriately rescaled pointwise maxima of independent replications of a field. The most commonly used parametric max-

stable models are the Smith (Smith, 1990), Schlather (Schlather, 2002), Brown–Resnick (Brown and Resnick, 1977; Kabluchko et al., 2009) and extremal-t (Opitz, 2013) models. Although many models for time-varying marginal (GEV) parameters have been proposed (e.g, Davison et al., 2013, and references therein), to our knowledge, no model for time-varying dependence structure has been developed in the spatial extremes context. Thus, our model fills a gap in the literature while allowing us to deal with a significant practical problem. In the multivariate setting, this issue was tackled by Mhalla et al. (2017), who used a generalized additive model to introduce covariates into the Pickands dependence function (Pickands, 1981) of a max-stable random vector. The modelling of spatial non-stationarity (as opposed to temporal non-stationarity) in the dependence structure of max-stable fields has received slightly more attention. Smith and Stephenson (2009) allowed the covariance matrix of the Smith model to vary across space, whereas Huser and Genton (2016) extended the extremal-t model by taking non-stationary correlation functions for the underlying Gaussian random field, and proposed a max-mixture of max-stable models with spatially dependent weights. Space-varying covariates such as longitude, latitude and elevation, can be incorporated into the correlation functions and the weights.

In our space-time model, when the Brown–Resnick or extremal-t fields are used, we propose to let the parameters (range, smoothness and possible anisotropy parameters) of the variogram or correlation function of their underlying Gaussian field depend on covariates through a general regression function that may involve splines or wavelets. In our application, the time step corresponds to one month and we choose a fractional Brown–Resnick field whose range depends on ENSO and month through a tensor product spline. Such a spline basis captures the interactions between the covariates and allows the ENSO effect to vary from one month to the next. We fit our model using pairwise likelihood (e.g., Padoan et al., 2010) and show by simulation that all parameters can be estimated rather accurately. Furthermore, the out-sample performance of our model is good and our findings have broad meteorological explanations. The range parameter tends to be lower

in summer and higher during El Niño events, indicating that the extreme events of PROD, CAPE and SRH are more localized in summer and more spatially extended during phases of positive ENSO.

We also contribute new methods for inference on max-stable fields. In environmental applications, data may exhibit asymptotic independence, in which case max-stable fields are unsuitable, and several subasymptotic models have been proposed to alleviate this (e.g., Huser and Wadsworth, 2019; Huser et al., 2021). One should always assess the validity of max-stable models in applications, and Gabda et al. (2012) and Buhl and Klüppelberg (2016) proposed graphical diagnostics for data with standardized margins. Here we develop a max-stability test that accounts for the unknown margins encountered in practice by approximating the distribution of a specific test statistic under the null hypothesis of max-stability using the bootstrap, and propose a strategy for choosing the validation dataset. Owing to the complexity of our model and the large number of grid points considered, simultaneous estimation of the marginal (GEV) parameters and the dependence parameters of the max-stable field is computationally too intensive, and so we fit the model in two steps: we estimate the GEV parameters, transform the data to standard Fréchet margins and then fit the dependence parameters using pairwise likelihood. We demonstrate that, following a two-step procedure, the sandwich matrix gives poor confidence intervals, whereas the non-parametric bootstrap gives better coverage. We also show that in such a context model selection using the composite likelihood information criterion (Padoan et al., 2010) is sub-optimal and propose a better criterion using a bootstrap-based estimator of the non-normalized composite Kullback–Leibler divergence.

The rest of the paper is organized as follows. In Section 2, we outline max-stable fields and their estimation by pairwise likelihood, and present the data and some exploratory analyses. Section 3 details our main methodological contributions: the model, the max-stability test, and the bootstrap-based model selection criterion. Section 4 is dedicated to the case study: we apply the model and methodologies developed in Section 3 to the

thunderstorm environment data. Section 5 summarizes our main contributions and findings and gives some future perspectives. Throughout the paper, $\mathcal{X}$ denotes a subset of $\mathbb{R}^2$, and $\overset{d}{=}$ and $\overset{d}{\to}$ denote equality and convergence in distribution, respectively; in the case of random fields, these should be understood as applying to all finite-dimensional distributions.

2 Preliminaries

2.1 Max-stable random fields

A random field $\{G(\boldsymbol{s}) : \boldsymbol{s} \in \mathcal{X}\}$ is said to be max-stable if there exist sequences of functions $\{a_n(\boldsymbol{s}), \boldsymbol{s} \in \mathcal{X}\}_{n\geq 1} > 0$ and $\{b_n(\boldsymbol{s}), \boldsymbol{s} \in \mathcal{X}\}_{n\geq 1} \in \mathbb{R}$ such that, for any $n \geq 1$,

$$\left\{ \frac{\max_{i=1}^n G_i(\boldsymbol{s}) - b_n(\boldsymbol{s})}{a_n(\boldsymbol{s})} : \boldsymbol{s} \in \mathcal{X} \right\} \overset{d}{=} \{G(\boldsymbol{s}) : \boldsymbol{s} \in \mathcal{X}\},$$

where $G_1, \ldots, G_n$ are independent replicates of G. Let $\tilde{T}_1, \ldots, \tilde{T}_n$, be independent replications of a random field $\{\tilde{T}(\boldsymbol{s}) : \boldsymbol{s} \in \mathcal{X}\}$. Let $\{c_n(\boldsymbol{s}), \boldsymbol{s} \in \mathcal{X}\}_{n\geq 1}$ and $\{d_n(\boldsymbol{s}), \boldsymbol{s} \in \mathcal{X}\}_{n\geq 1}$ be sequences of functions that respectively take values in the strictly positive and real numbers. If there exists a non-degenerate random field $\{G(\boldsymbol{s}) : \boldsymbol{s} \in \mathcal{X}\}$ such that

$$\left\{ \frac{\max_{i=1}^n \tilde{T}_i(\boldsymbol{s}) - d_n(\boldsymbol{s})}{c_n(\boldsymbol{s})} : \boldsymbol{s} \in \mathcal{X} \right\} \overset{d}{\to} \{G(\boldsymbol{s}) : \boldsymbol{s} \in \mathcal{X}\}, \quad n \to \infty, \tag{1}$$

then G must be max-stable (de Haan, 1984), and this explains the relevance of max-stable fields as models for the pointwise maxima of random fields. If $\{G(\boldsymbol{s}) : \boldsymbol{s} \in \mathcal{X}\}$ is a max-stable field, then, for any $\boldsymbol{s} \in \mathcal{X}$, $G(\boldsymbol{s})$ has a GEV distribution (e.g., Coles, 2001, Section 3.1) with location, scale and shape parameters $\eta_{\boldsymbol{s}}$, $\tau_{\boldsymbol{s}}$ and $\xi_{\boldsymbol{s}}$. The transformed variable $Z(\boldsymbol{s}) = [1 + \xi_{\boldsymbol{s}}\{G(\boldsymbol{s}) - \eta_{\boldsymbol{s}}\}/\tau_{\boldsymbol{s}}]^{1/\xi_{\boldsymbol{s}}}$ is standard Fréchet distributed, i.e., $\mathbb{P}(Z(\boldsymbol{s}) \leq z) = \exp(-1/z)$ for $z > 0$; max-stable fields having standard Fréchet margins are said to be simple. Max-stable fields are sometimes instead standardized to have Gumbel margins; the Gumbel distribution function with location parameter μ is $\exp[-\exp\{-(x-\mu)\}]$, $x \in \mathbb{R}$, and the standard Gumbel distribution appears when $\mu = 0$.

Any simple max-stable field can be represented as (de Haan, 1984)

$$Z(\boldsymbol{s}) = \max_{i=1}^{\infty} R_i U_i(\boldsymbol{s}), \quad \boldsymbol{s} \in \mathcal{X}, \tag{2}$$

where the $(R_i)_{i\geq 1}$ are the points of a Poisson point process on $(0, \infty)$ with intensity function $r^{-2}\mathrm{d}r$ and the $(U_i)_{i\geq 1}$ are independent replicates of a non-negative random field $\{U(\boldsymbol{s}), \boldsymbol{s} \in \mathcal{X}\}$ such that $\mathrm{E}\{U(\boldsymbol{s})\} = 1$ for any $\boldsymbol{s} \in \mathcal{X}$. Any field defined by (2) is simple max-stable, moreover, and this allows parametric max-stable fields to be constructed, such as the Smith (1990), Schlather (2002), Brown–Resnick (Brown and Resnick, 1977; Kabluchko et al., 2009), and extremal-t (Opitz, 2013) models. The last two are flexible and have been found to capture extremes well, and in Section 4 we use the Brown–Resnick model.

Write $W(\boldsymbol{s}) = \exp\left[\varepsilon(\boldsymbol{s}) - \mathrm{Var}\{\varepsilon(\boldsymbol{s})\}/2\right]$, $\boldsymbol{s} \in \mathcal{X}$, where Var denotes variance, and $\{\varepsilon(\boldsymbol{s}) : \boldsymbol{s} \in \mathcal{X}\}$ is a centred Gaussian random field with stationary increments and semivariogram γ. Using $U = W$ in (2) leads to the Brown–Resnick random field associated with the semivariogram γ. A frequently-used isotropic semivariogram is $\gamma(\boldsymbol{s}) = (\|\boldsymbol{s}\|/\rho)^{\alpha}$, $\boldsymbol{s} \in \mathcal{X}$, where $\rho > 0$ and $\alpha \in (0, 2]$ are the range and smoothness parameters, respectively, and $\|\cdot\|$ is the Euclidean distance. An unbounded semivariogram such as this yields a field that is mixing (by Theorem 3.1 in Kabluchko and Schlather, 2010), which is appropriate if the extreme events are spatially localized. As pointwise maxima typically arise from several individual events, the spatial scale of dependence in the field of such maxima reflects the spatial extent of the individual extreme events (e.g., Dombry et al., 2018). Thus the range parameter can be interpreted in terms of the characteristic size of individual extreme events, whereas the smoothness parameter controls the regularity of the field's sample paths. We will account for possible geometric anisotropy by using the semivariogram

$$\gamma(\boldsymbol{s}) = (\|A\boldsymbol{s}\|/\rho)^{\alpha}, \quad \boldsymbol{s} \in \mathcal{X}, \tag{3}$$

where

$$A = \begin{pmatrix} \cos\kappa & -\sin\kappa \\ r\sin\kappa & r\cos\kappa \end{pmatrix}, \tag{4}$$

with scaling and rotation parameters respectively $r > 0$ and $\kappa \in [0, \pi]$; Blanchet and Davison (2011) used this idea to introduce anisotropy into the Schlather model.

The Schlather and extremal-t models are also typically parametrized by a range parameter $\rho > 0$ and smoothness parameter $\alpha \in (0, 2]$ through the isotropic correlation function C of their underlying standard Gaussian field; the powered exponential, Cauchy and Whittle-Matérn correlation functions are common in applications. In anisotropic cases we consider $C(\|A\boldsymbol{s}\|)$ instead of $C(\|\boldsymbol{s}\|)$, and then the correlations also depend on r and κ.

For any simple max-stable field, we have, for $\boldsymbol{s}_1, \ldots, \boldsymbol{s}_D \in \mathcal{X}$ and $z_1, \ldots, z_D > 0$,

$$\mathbb{P}\{Z(\boldsymbol{s}_1) \leq z_1, \ldots, Z(\boldsymbol{s}_D) \leq z_D\} = \exp\left\{-V_{\boldsymbol{s}_1,\ldots,\boldsymbol{s}_D}(z_1, \ldots, z_D)\right\}, \tag{5}$$

with (Pickands, 1981)

$$V_{\boldsymbol{s}_1,\ldots,\boldsymbol{s}_D}(z_1, \ldots, z_D) = \int_{\mathcal{S}_D} \max\left\{\frac{w_1}{z_1}, \ldots, \frac{w_D}{z_D}\right\} \mathrm{d}M_{\boldsymbol{s}_1,\ldots,\boldsymbol{s}_D}(w_1, \ldots, w_D),$$

where $M_{\boldsymbol{s}_1,\ldots,\boldsymbol{s}_D}$ is a measure on the D-dimensional simplex $\mathcal{S}_D$ satisfying

$$\int w_d \, \mathrm{d}M_{\boldsymbol{s}_1,\ldots,\boldsymbol{s}_D}(w_1, \ldots, w_D) = 1,$$

for each $d \in \{1, \ldots, D\}$. The function $V_{\boldsymbol{s}_1,\ldots,\boldsymbol{s}_D}$, called the exponent measure of the max-stable random vector $(Z(\boldsymbol{s}_1), \ldots, Z(\boldsymbol{s}_D))'$, entirely characterizes its dependence and is homogeneous of order -1; the $'$ denotes transposition of a vector. Several summaries of the dependence (so-called dependence measures) have been proposed for max-stable fields/vectors, one being the extremal coefficient (Schlather and Tawn, 2003). If Z is a simple max-stable field, then the bivariate distribution function satisfies

$$\mathbb{P}(Z(\boldsymbol{s}_1) \leq u, Z(\boldsymbol{s}_2) \leq u) = \exp\left\{-\frac{\theta(\boldsymbol{s}_1, \boldsymbol{s}_2)}{u}\right\}, \quad \boldsymbol{s}_1, \boldsymbol{s}_2 \in \mathcal{X}, \tag{6}$$

where $u > 0$ and $\theta(\boldsymbol{s}_1, \boldsymbol{s}_2)$ is the bivariate extremal coefficient. By homogeneity of the exponent measure, $\theta(\boldsymbol{s}_1, \boldsymbol{s}_2) = V_{\boldsymbol{s}_1,\boldsymbol{s}_2}(1, 1)$. Furthermore, $\theta(\boldsymbol{s}_1, \boldsymbol{s}_2) \in [1, 2]$ for any $\boldsymbol{s}_1, \boldsymbol{s}_2 \in \mathcal{X}$, with values 1 and 2 indicating perfect dependence and independence, respectively. The lower the value of $\theta(\boldsymbol{s}_1, \boldsymbol{s}_2)$, the higher the dependence. The pairwise extremal coefficient

has a one-to-one relation with the F-madogram (Cooley et al., 2006) and this allows it to be estimated non-parametrically. If Z in (6) is a Brown–Renick field associated with the semivariogram γ, then (e.g., Davison et al., 2012)

$$\theta(\boldsymbol{s}_1, \boldsymbol{s}_2) = 2\Phi\left\{\sqrt{\gamma(\boldsymbol{s}_2 - \boldsymbol{s}_1)}/2\right\}, \quad \boldsymbol{s}_1, \boldsymbol{s}_2 \in \mathcal{X}, \tag{7}$$

where Φ denotes the standard univariate Gaussian distribution function.

If $\{Z(\boldsymbol{s}) : \boldsymbol{s} \in \mathcal{X}\}$ is a simple max-stable field, then (e.g., Davison et al., 2012)

$$\lim_{z \to \infty} \Pr\{Z(\boldsymbol{s}_1) > z \mid Z(\boldsymbol{s}_2) > z\} = 2 - \theta(\boldsymbol{s}_1, \boldsymbol{s}_2), \quad \boldsymbol{s}_1, \boldsymbol{s}_2 \in \mathcal{X}. \tag{8}$$

Thus, unless Z is standard Fréchet white noise, there exist $\boldsymbol{s}_1, \boldsymbol{s}_2$ such that the limit in (8) is strictly positive and therefore Z is asymptotically dependent. A possible way to assess the suitability of max-stable models consists in testing whether the left hand-side of (8) vanishes for different pairs of grid points, e.g., using the tests reviewed by de Carvalho and Ramos (2012); see for instance Bacro et al. (2010). However, evidence of asymptotic dependence does not entail suitability of max-stable models, as data may show asymptotic dependence without being max-stable. In this paper, we instead explicitly test the null hypothesis of max-stability; see Section 3.2.

2.2 Estimation of max-stable fields

Let $\boldsymbol{s}_1, \ldots, \boldsymbol{s}_D \in \mathcal{X}$ denote grid points at which we regularly observe a field of pointwise maxima, which, based on (1), we model by a max-stable field. In Section 3.1.2 we shall justify modelling the margin at grid point $\boldsymbol{s}_d$ by a GEV distribution with location, scale and shape parameters $\eta_{\boldsymbol{s}_d}$, $\tau_{\boldsymbol{s}_d}$ and $\xi_{\boldsymbol{s}_d}$. In our setting this entails the estimation of $3 \times D$, i.e., 1857, parameters. Computational considerations make it usual to first estimate these marginal parameters by maximum likelihood, and then to fix them and estimate the dependence parameters of the max-stable field by maximizing the composite log-likelihood.

The D-dimensional multivariate density of a max-stable random field can be intractable, as the exponent measure in (5) can be difficult to characterize unless D is small and the

exponential leads to a combinatorial explosion of the number of terms in the density. Full likelihood inference is thus out of reach in many cases and so composite likelihood techniques (e.g., Varin et al., 2011) have been extensively used. Pairwise composite likelihoods are most common (e.g., Padoan et al., 2010; Blanchet and Davison, 2011; Davison et al., 2012), but higher order composite likelihoods have also been considered (e.g., Huser and Davison, 2013; Castruccio et al., 2016). Under mild regularity conditions, the maximum pairwise likelihood estimator is strongly consistent and asymptotically normal but it has a larger variance than the maximum likelihood estimator. Padoan et al. (2010) and Sang and Genton (2014) showed that truncating the pairwise likelihood by ignoring pairs of sites that are far apart can improve its statistical efficiency; for similar findings in other settings, see the references in Sang and Genton (2014). Ignoring some pairs also decreases the computational burden, which is valuable for large values of D, such as our $D = 619$. Castruccio et al. (2016) showed that truncation increases statistical efficiency by more for pairwise or triplewise likelihoods than for higher order composite likelihoods.

Let $z_{\boldsymbol{s},t}$ denote the maximum at $\boldsymbol{s}$ during the t-th period, transformed marginally to standard Fréchet, let $\boldsymbol{\psi}$ denote the vector of dependence parameters of the max-stable model, and let $f_{\boldsymbol{s}_d,\boldsymbol{s}_{d'};\boldsymbol{\psi}}$ denote the corresponding pairwise density for grid points $\boldsymbol{s}_d, \boldsymbol{s}_{d'} \in \mathcal{X}$. The truncated pairwise log-likelihood is

$$l(\boldsymbol{\psi}) = \sum_{t=1}^{T} \sum_{d=1}^{D-1} \sum_{d'=d+1}^{D} \mathbb{I}_{\left\{||\boldsymbol{s}_d - \boldsymbol{s}_{d'}|| \leq \sqrt{2c^2}\right\}} \log f_{\boldsymbol{s}_d,\boldsymbol{s}_{d'};\boldsymbol{\psi}}(z_{\boldsymbol{s}_d,t}, z_{\boldsymbol{s}_{d'},t}), \tag{9}$$

where c is the truncation parameter and $\mathbb{I}_{\{\cdot\}}$ is the indicator function. Choosing truncation distance $\sqrt{2c^2}$ rather than c allows us to take pairs of sites along the diagonals into account.

We chose a value of c adapted to the context of our work by simulating Brown–Resnick fields having semivariogram (3) with $r = 1$, $\kappa = 0$, $\alpha = 1$ and $\rho \in \{1, 2, 4, 8, 12\}$, on squares containing 25, 100, and 225 grid points. In each of these 15 settings, we simulated 444 (the number of months in our data) independent realizations of the field 400 times independently. For each of these 400 experiments, we estimated ρ using the truncated pairwise log-likelihood (9) with $c \in \{1, 2, 3, 4\}$. The smoothness parameter $\alpha = 1$ and

scaling and rotation parameters $r = 1$ and $\kappa = 0$, are close to the estimates from our data. We let the range ρ and the spatial domain vary as the optimal truncation distance depends on both. Our results (Figure 7 in the Supplementary Material) show that estimation becomes more precise when ρ decreases and D increases. In most settings $c = 2$ leads to more precise estimation, and we use this value below.

2.3 Data and exploratory analysis

The data we study were used in Koch et al. (2021) and constitute a coarse version of reanalysis data from the North American Regional Reanalysis (NARR). They consist of 3-hourly time-series of 0–180 hPa CAPE (J kg^{-1}) and 0–3 km SRH (m^2 s^{-2}) from 1 January 1979 at 00:00 Coordinated Universal Time (UTC) to 31 December 2015 at 21:00 UTC. For consistency, we dropped any data for February 29; this does not impact our findings. The area considered is a rectangle over the contiguous US from $-110°$ to $-80°$ longitude and $30°$ to $50°$ latitude (see Figure 2), thus containing Tornado Alley (Texas, Oklahoma, Kansas, Nebraska, Iowa and South Dakota), the riskiest region of the US in terms of severe thunderstorms. The resolution is $1°$ longitude and $1°$ latitude, leading to 651 grid points in our region; no data are available for 32 grid points over water. We use the time series of CAPE and SRH to build 3-hourly time series of PROD $= \sqrt{\text{CAPE}} \times \text{SRH}$ (m^3 s^{-3}). Finally, as a measure of ENSO, we use monthly values of the Niño-3.4 index (°C) from 1979 to 2015, taken from the ERSSTv5 data set publicly available from the National Oceanic and Atmospheric Administration (NOAA) Climate Prediction Center.

Figure 1 shows that for PROD maxima in April, the bivariate extremal coefficient tends to be lower during El Niño episodes than during periods with low absolute value of ENSO, indicating that the spatial dependence in the field of pointwise maxima increases during El Niño events. This may result from an increase of the spatial extent of individual PROD events, which is plausible as large ENSO values are associated with a weaker north-south temperature gradient over the US; see Section 4.4. Similarly, the extremal coefficients are

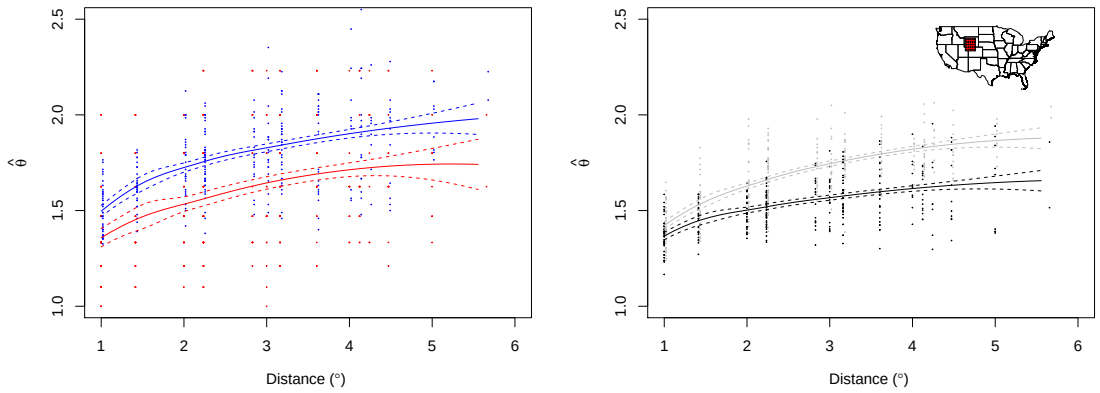


Figure 1: The dots show the empirical pairwise extremal coefficients for PROD using all grid points in the square from $-110°$ to $-106°$ longitude and $40°$ to $44°$ latitude (indicated by the red region on the map in the right panel). The solid lines depict the best local polynomial regression curves and the dotted lines characterize the associated 95% pointwise confidence intervals (assuming that the estimates are known). The left panel concerns April maxima for ENSO $> 0.5°$C (red) and $|\text{ENSO}| \leq 0.5°$C (blue), and the right panel concerns January (black) and July (grey) maxima.

lower in January than in July, suggesting wider PROD events, agreeing with the fact that convective weather events are more localized in summer than in winter. These findings are true for regions other than that considered in Figure 1 (not shown) and suggest the use of ENSO and month as covariates for the range parameter.

3 Novel methodology

3.1 Model

3.1.1 General case

We propose a space-time model that is simple max-stable at each time point. Let T be the number of time points and let $\boldsymbol{x}_t = (x_{1,t}, \ldots, x_{p,t})'$, $t = 1, \ldots, T$, gather the observations of p covariates at time t, e.g., large-scale atmospheric signals or the month associated with time t. Our space-time model $\{Z(\boldsymbol{s}, t) : \boldsymbol{s} \in \mathcal{X}, t = 1, \ldots, T\}$ is then defined as follows:

1. for any $t = 1, \ldots, T$, the spatial field $\{Z(\boldsymbol{s}, t) : \boldsymbol{s} \in \mathcal{X}\}$ is max-stable with a spatial

dependence structure involving the vector of covariates $\boldsymbol{x}_t$;

2. the spatial fields $\{Z(\boldsymbol{s},1):\boldsymbol{s}\in\mathcal{X}\},\ldots,\{Z(\boldsymbol{s},T):\boldsymbol{s}\in\mathcal{X}\}$ are independent.

As mentioned in Section 2.1, max-stable models typically depend on range and smoothness parameters $\rho>0$ and $\alpha\in(0,2]$, a scaling parameter $r>0$ and a rotation parameter $\kappa\in[0,\pi]$. The value of a parameter a_t at time t may depend on the $\boldsymbol{x}_t$ through a linear basis function, viz

$$g(a_t)=\sum_{k=1}^{K}\beta_k h_k(\boldsymbol{x}_t), \tag{10}$$

where g is a monotonic link function, $K\in\mathbb{N}\backslash\{0\}$, $h_1,\ldots,h_K$ are functions from $\mathbb{R}^p$ to $\mathbb{R}$, and the β_k are real numbers. A natural choice for g in the case of ρ is the logarithm, but other choices would be necessary for the other parameters. Depending on the choice of h_k, (10) can represent a generalized linear model or a more flexible and non-linear model (e.g., with splines or wavelets). Radial cubic splines are useful for continuous variables such as weather variables (e.g., ENSO), cyclic P-splines are appropriate when using the month as covariate, as they allow a smooth transition between the first and the last month, and tensor product splines can capture interactions between different covariates. The simultaneous modelling of several parameters with (10) requires enough data, as it can be hard to detect non-stationarity in the dependence structure. For instance, modelling both ρ and α in this way is difficult because their effects may be difficult to distinguish.

3.1.2 Specification for the case study, and simulations

Finding appropriate and parsimonious trend surfaces for the marginal parameters is challenging for large and meteorologically heterogeneous regions. Using ill-specified trend surfaces may bias our characterization of the dependence structure, so we model the monthly maxima by fitting GEV distributions separately at each grid point and then model the field obtained after using these separate fits to transform the data to standard Fréchet margins. Our space-time model for these transformed data lies in the class of max-stable models introduced in Section 3.1.1; we use the Brown–Resnick model with variogram (3),

which often fits environmental extremes well (e.g., Davison et al., 2012). Fitting a classical Brown–Resnick model for each month separately showed no evidence of month- or ENSO-specific smoothness, scaling and rotation parameters, for PROD, CAPE or SRH (not shown). Thus, based on our exploratory analysis (Figure 1) and meteorological understanding, we model the range parameter ρ as in (10) with ENSO and month as covariates, keep the parameters α, r and κ constant, and take the time step to be one month ($t = 1$ corresponds to 31 January 1979 23:00 UTC, $t = 2$ to 28 February 1979 23:00 UTC, ...). Our vector of covariates at t is therefore

$$\boldsymbol{x}_t = (\mathrm{ENSO}_t, t \bmod 12)', \quad t = 1, \ldots, 444, \tag{11}$$

where ENSO_t is the value of ENSO for the month associated with t, and mod denotes the modulo operation. The effect of these covariates on ρ appears to be non-linear (see, e.g., Hoerling et al., 1997, regarding the non-linearity of general responses to El Niño and La Niña), and the covariates interact, so we choose the functions h_k as the components of a tensor product spline basis between a radial cubic spline basis in the ENSO direction and a cyclic P-spline basis in the month direction, allowing us to borrow strength from neighbouring ENSO states and months. Thus our final model at time $t = 1, \ldots, T$, for the standardized quantities is the Brown–Resnick field with semivariogram

$$\gamma(\boldsymbol{s}, t) = \left[\frac{\|A\boldsymbol{s}\|}{\exp\left\{\sum_{k=1}^{K} \beta_k h_k(\boldsymbol{x}_t)\right\}} \right]^{\alpha}, \quad \boldsymbol{s} \in \mathcal{X}, \tag{12}$$

where A is the matrix (4) with $r > 0$ and $\kappa \in [0, \pi]$. To choose the knots, we fit models with different numbers of knots positioned regularly in each direction and then choose the best using the bootstrap-based selection criterion developed in Section 3.4.

We checked by simulation that the model parameters are identifiable and can be estimated adequately in a setting similar to the case study. Such verification is especially important for the model in (12) owing to its complexity and the large number of parameters, and since detecting non-stationarity in the extremal dependence structure is challenging with too few data. We consider (12) with $T = 444$ on a square containing 625 grid points

and with parameters $r = 0.72$, $\kappa = -0.08$, and $\alpha = 1.26$, three knots with coordinates -1.06, 0.05, 1.16 in the ENSO direction (the 0.1 and 0.9 quantiles of observed ENSO values and their mid-point), and knots at 0.5, 4.5, 8.5, 12.5 in the month direction. As we use a circular P spline basis for months, the values of the spline are the same at 0.5 and 12.5, giving three distinct knots in both the ENSO and month directions, i.e., nine knots over the space of covariates. The corresponding coefficients, $\beta_0 = 0.52$ (intercept), $\beta_1 = -0.03$, $\beta_2 = 0.02$, $\beta_3 = 0.07$, $\beta_4 = 0.11$, $\beta_5 = -0.07$, $\beta_6 = -0.23$, $\beta_7 = -0.03$, $\beta_8 = 0.02$ and $\beta_9 = 0.04$, correspond to those obtained when fitting this model to the data described in Section 2.3. We estimate all the parameters for 100 independent replicates of this model. Figure 8 (Supplementary Material) suggests that all the estimators are essentially unbiased and that all parameters are recovered well, but that the estimators of the parameters associated with the spline basis tend to more variable than are those for the others. The smoothness parameter α and the scaling factor r are very well estimated. Figure 9 (Supplementary Material) also shows that signals and non-signals are equally well-identified.

3.2 A max-stability test with unknown margins

Assume that a max-stable field with standard Gumbel margins, $\{Z(\boldsymbol{s}) : \boldsymbol{s} \in \mathcal{X}\}$ is observed in a testing region $\mathcal{T} \subseteq \mathcal{X}$ consisting of grid points $\{\boldsymbol{s}_1, \ldots, \boldsymbol{s}_D\}$, and let $\mathcal{S} = \{1, \ldots, D\}$. The homogeneity of order -1 of the exponent measure in (5) implies that $Z_{\mathcal{S}} = \max_{d \in \mathcal{S}} Z(\boldsymbol{s}_d)$ has a Gumbel distribution with location parameter $\mu_{\mathcal{S}} = \log V_{\boldsymbol{s}_d, d \in \mathcal{S}}$, where $V_{\boldsymbol{s}_d, d \in \mathcal{S}}$ is the exponent measure of $\{Z(\boldsymbol{s}_d), d \in \mathcal{S}\}$. Gabda et al. (2012) and Buhl and Klüppelberg (2016) compared the empirical distribution of $Z_{\mathcal{S}}$ and a Gumbel distribution whose location $\hat{\mu}_{\mathcal{S}}$ has been estimated from simulated realizations of $Z_{\mathcal{S}}$.

In applications we must transform data to Gumbel margins before performing such a test. We use an Anderson–Darling statistic to measure the distance between the empirical distribution of $Z_{\mathcal{S}}$ and a Gumbel distribution with location $\hat{\mu}_{\mathcal{S}}$ and thus to assess the null hypothesis that the multivariate distribution is max-stable. The null distribution should

allow for the estimation of both $\mu_{\mathcal{S}}$ and the margins, and we use the bootstrap to do so.

Our proposed bootstrap test is parametric for the margins and non-parametric for the dependence, on which we do not wish to impose a particular model. Let $(z^\star_{1,m}, \ldots, z^\star_{D,m})'$ denote the vector of the m-th observed maxima at all grid points in $\mathcal{S}$, where $m \in \{1, \ldots, M\}$. For each grid point $d \in \mathcal{S}$, we first fit the GEV distribution using $z^\star_{d,1}, \ldots, z^\star_{d,M}$ to obtain estimators $\hat{\eta}^\star_d$, $\hat{\tau}^\star_d$ and $\hat{\xi}^\star_d$. We approximate the distribution of the Anderson–Darling statistic under the null hypothesis of max-stability by B independent replications of the following procedure:

1. use the empirical likelihood (Owen, 2001) approach outlined in the Supplementary Material to simulate M replicates of a max-stable vector, denoted $(\tilde{z}_{1,1}, \ldots, \tilde{z}_{D,1})', \ldots, (\tilde{z}_{1,M}, \ldots, \tilde{z}_{D,M})'$, such that $\tilde{z}_{d,1}, \ldots, \tilde{z}_{d,M}$, $d \in \mathcal{S}$, are drawn from a GEV distribution with location, scale and shape parameters $\hat{\eta}^\star_d$, $\hat{\tau}^\star_d$ and $\hat{\xi}^\star_d$;

2. for each $d \in \mathcal{S}$, use a GEV distribution fitted to $\tilde{z}_{d,1}, \ldots, \tilde{z}_{d,M}$ by maximum likelihood to transform the $\tilde{z}_{d,m}$ to approximately standard Gumbel-distributed quantities $z_{d,1}, \ldots, z_{d,M}$, yielding $(z_{1,1}, \ldots, z_{D,1})', \ldots, (z_{1,M}, \ldots, z_{D,M})'$;

3. compute $z_{\mathcal{S},m} = \max_{d \in \mathcal{S}} z_{d,m}$ $(m = 1, \ldots, M)$ and fit a Gumbel distribution to $z_{\mathcal{S},1}, \ldots, z_{\mathcal{S},M}$ using maximum likelihood, giving location parameter estimate $\hat{\mu}_{\mathcal{S}}$;

4. calculate the Anderson–Darling statistic measuring the distance between the empirical distribution of the $z_{\mathcal{S},1}, \ldots, z_{\mathcal{S},M}$ and a Gumbel distribution with location $\hat{\mu}_{\mathcal{S}}$.

The same test might be applied with $\mathcal{S}$ any subset of $\{1, \ldots, D\}$ of size two or more.

We perform two experiments with $D = 25$ and $M = 40$ block maxima of size 240. We first generate from a multivariate logistic extreme-value distribution

$$G(y_1, \ldots, y_D) = \exp\left\{ -\left(\sum_{d=1}^{D} y_d^{-1/\lambda} \right)^{\lambda} \right\}, \quad y_1, \ldots, y_D > 0,$$

with dependence parameter $\lambda \in \{0.1, 0.5, 0.9\}$, and perform our max-stability test on these observations with $B = 200$. We then repeat this experiment with data from a multivariate

Gaussian distribution with common pairwise correlation $\zeta \in \{0.1, 0.5, 0.9, 0.99\}$. To assess the empirical size and power of the test, we replicate both experiments 1000 times. Pointwise maxima of Gaussian fields converge in (1) to the degenerate independent max-stable field, but a block size of 240 is insufficient for convergence, so using the multivariate normal distribution is an approximate but reasonable way to assess the power of our test.

Table 4 in the Supplementary Material shows that the empirical size of the test is controlled reasonably well in this setting, with the 1000 Anderson-Darling and Kolmogorov-Smirnoff p-values correctly showing no departure from uniformity at the 5% level for the logistic models, which are max-stable. All tests for uniformity of the p-values are rejected at the 5% level for the multivariate normal cases. The power rises first as dependence increases, but falls when $\zeta = 0.99$, probably because the simulated empirical distributions are then very close to the perfectly dependent max-stable distribution. The power is also low when $\zeta = 0.1$, perhaps because the empirical distributions are then close to the independent max-stable distribution. Figure 10, which shows quantile-quantile plots of the p-values in two simulation settings, illustrates the departure from uniformity in the Gaussian case.

3.3 Selection of data used for validation

A validation set is a subset of the data that is not used to fit the model but to assess its performance. In spatial extremes, the validation set often consists of time series at randomly chosen grid points (e.g., Davison et al., 2012; Huser and Wadsworth, 2019). We propose a new approach that we first present in a general setting. Assume that we have data, a statistical model that relies on a specific assumption (here, max-stability), and a statistical test capable of detecting non-suitability of that assumption in different subsets of the data. We take as validation set several or all subsets of the whole dataset for which the test rejects the validity of that assumption. The model is thus fitted to the data that are the most compatible with the underlying assumption, and assessed on those which are the least compatible with it. This quantifies the model's performance in the worst case, so

satisfactory results on this validation set (as in Section 4.3) support the suitability of the model for other out-sample data, though poor validation results need not imply that the model is inadequate overall. This approach is particularly suited to heterogeneous data, for which more usual methods may be inconclusive.

In our case study, we split the region into small rectangles termed windows and, for each variable, we apply for each month the max-stability test of Section 3.2 to each window; we take $\mathcal{T}$ to be the corresponding window. For each variable, our validation set then consists of the data at grid and time points belonging to window-month combinations where the null hypothesis of max-stability is rejected.

3.4 Bootstrap-based uncertainty assessment and model selection

Let $\mathcal{Y} = (\boldsymbol{Y}_1, \ldots, \boldsymbol{Y}_T)'$ be a data matrix, where $\boldsymbol{Y}_1, \ldots, \boldsymbol{Y}_T$ are independent replicates of a D-dimensional random vector $\boldsymbol{Y}$, such as the vector of maxima at certain grid points at a given time, and suppose that the margins of $\boldsymbol{Y}$ have been estimated. In this section we discuss uncertainty quantification and model selection when using composite likelihood to estimate the dependence structure.

Suppose we have a parametric model for each margin of $\boldsymbol{Y}$ and that the marginal parameters of all components of $\boldsymbol{Y}$ are gathered in $\boldsymbol{\lambda}$. Below, we consider both the ideal situation where the exact marginal models and $\boldsymbol{\lambda}$ are known, and the more realistic situation where $\boldsymbol{\lambda}$ is estimated by $\hat{\boldsymbol{\lambda}}$ prior to dependence modelling. Let the function $t_{\boldsymbol{\lambda}}$ transform a data matrix to have known margins, let $\boldsymbol{Z}_1, \ldots, \boldsymbol{Z}_T$ and $\boldsymbol{Z}$ be transformations of $\boldsymbol{Y}_1, \ldots, \boldsymbol{Y}_T$ and $\boldsymbol{Y}$ to have known margins, and let $\mathcal{Z} = (\boldsymbol{Z}_1, \ldots, \boldsymbol{Z}_T)'$. Then $\mathcal{Z} = t_{\boldsymbol{\lambda}}(\mathcal{Y})$ if $\boldsymbol{\lambda}$ is known and $\mathcal{Z} = t_{\hat{\boldsymbol{\lambda}}}(\mathcal{Y})$ if $\boldsymbol{\lambda}$ is estimated by $\hat{\boldsymbol{\lambda}}$.

Assume that we model $\mathcal{Z}$ using a family $\mathcal{F} = \{f(\boldsymbol{z}, \boldsymbol{\psi}) : \boldsymbol{z} \in \mathbb{R}^D, \boldsymbol{\psi} \in \Psi \subseteq \mathbb{R}^p\}$ of density functions with known margins (typically standard Fréchet in the spatial extremes setting) and dependence parameter $\boldsymbol{\psi}$. The composite likelihood is $L_C(\boldsymbol{\psi}; \mathcal{Z}) = \prod_{t=1}^{T} f_C(\boldsymbol{\psi}; \boldsymbol{Z}_t)$, where f_C is defined through the density f and characterizes the composite likelihood (see,

e.g., Varin and Vidoni, 2005, Definition 1), and we write $\hat{\boldsymbol{\psi}}$ for the maximum composite likelihood estimator. In the case of the truncated pairwise likelihood (9), f_C is the sum over all pairs of tapered bivariate densities.

When the true marginal models and $\boldsymbol{\lambda}$ are known, under mild regularity assumptions, $\hat{\boldsymbol{\psi}} \mathrel{\dot\sim} \mathrm{N}_p\{\boldsymbol{\psi}, \mathrm{I}(\boldsymbol{\psi})^{-1}\}$ for T large, where the sandwich information matrix $\mathrm{I}(\boldsymbol{\psi}) = \mathrm{H}(\boldsymbol{\psi})\mathrm{J}(\boldsymbol{\psi})^{-1}\mathrm{H}(\boldsymbol{\psi})$ with $\mathrm{H}(\boldsymbol{\psi}) = \mathrm{E}\{-\nabla^2_{\boldsymbol{\psi}} \log L_C(\boldsymbol{\psi}; \mathcal{Z})\}$ and $\mathrm{J}(\boldsymbol{\psi}) = \mathrm{V}\{\nabla_{\boldsymbol{\psi}} \log L_C(\boldsymbol{\psi}; \mathcal{Z})\}$, $\nabla^2_{\boldsymbol{\psi}}$ and $\nabla_{\boldsymbol{\psi}}$ denote the Hessian and gradient operators with respect to $\boldsymbol{\psi}$, and V indicates the covariance matrix operator. Confidence intervals can be based on the estimated sandwich covariance matrix $\hat{\mathrm{H}}(\hat{\boldsymbol{\psi}})^{-1}\hat{\mathrm{J}}(\hat{\boldsymbol{\psi}})\hat{\mathrm{H}}(\hat{\boldsymbol{\psi}})^{-1}$ (Padoan et al., 2010), where

$$\hat{\mathrm{H}}(\hat{\boldsymbol{\psi}}) = -\nabla^2_{\boldsymbol{\psi}} \log L_C(\hat{\boldsymbol{\psi}}; \mathcal{Z}), \quad \hat{\mathrm{J}}(\hat{\boldsymbol{\psi}}) = \sum_{t=1}^{T} \{\nabla_{\boldsymbol{\psi}} \log f_C(\hat{\boldsymbol{\psi}}; \boldsymbol{Z}_t)\}\{\nabla_{\boldsymbol{\psi}} \log f_C(\hat{\boldsymbol{\psi}}; \boldsymbol{Z}_t)\}'.$$

After fitting several models in $\mathcal{F}$ using composite likelihood, it is standard to select that having the highest observed value of $\log L_C(\hat{\boldsymbol{\psi}}, \mathcal{Z}) - \mathrm{tr}\{\hat{\mathrm{J}}(\hat{\boldsymbol{\psi}})\hat{\mathrm{H}}(\hat{\boldsymbol{\psi}})^{-1}\}$ (Varin and Vidoni, 2005), or equivalently the lowest observed value of (Padoan et al., 2010)

$$\mathrm{CLIC} = -2 \log L_C(\hat{\boldsymbol{\psi}}, \mathcal{Z}) + 2\mathrm{tr}\{\hat{\mathrm{J}}(\hat{\boldsymbol{\psi}})\hat{\mathrm{H}}(\hat{\boldsymbol{\psi}})^{-1}\}, \tag{13}$$

where tr denotes the trace.

If $\boldsymbol{\lambda}$ has been estimated in a first step, as is often the case in spatial extremal analysis, then use of the estimated covariance matrix and CLIC for uncertainty assessment of $\hat{\boldsymbol{\psi}}$ and model selection within $\mathcal{F}$ does not account for estimating the marginal parameters $\boldsymbol{\lambda}$. In spatial extremes, the non-parametric bootstrap is often used for uncertainty assessment (Davison et al., 2013, 2018; Huser and Wadsworth, 2019), showing that researchers are aware of the shortcomings of using the estimated sandwich covariance matrix, but this cannot be said of using CLIC for model selection in a two-step setting. Many studies (e.g., Davison et al., 2013, 2018; Huser and Genton, 2016; Huser et al., 2021) do not allow for the estimation of the margins.

In order to account for the effect of marginal estimation on model selection when using composite likelihood, we propose bootstrap estimation of the non-normalized composite

Kullback–Leibler divergence (Varin and Vidoni, 2005). In Section 3.4.1 we consider that the margins are known and extend the results of Shibata (1997) and Cavanaugh and Shumway (1997) to the composite likelihood setting, and in Section 3.4.2 we define a criterion to account for the marginal effects. Section 3.4.3 illustrates the benefits of this method through a simulation study. For notational simplicity we suppress the dependence of $\mathcal{Y}$, $\mathcal{Z}$, and $\hat{\boldsymbol{\psi}}$ on T throughout. Although we deal with max-stable fields, our ideas are generally valid.

3.4.1 Known margins

We assume that $\boldsymbol{\lambda}$ in $t_{\boldsymbol{\lambda}}$ is known and we seek the best model for $\mathcal{Z} = t_{\boldsymbol{\lambda}}(\mathcal{Y})$ by estimating the non-normalized composite Kullback–Leibler divergence from a model to the truth using a non-parametric bootstrap, following what Cavanaugh and Shumway (1997) and Shibata (1997) did for the non-normalized Kullback–Leibler divergence.

Let $g(\boldsymbol{z})$, $\boldsymbol{z} \in \mathbb{R}^D$, be the true density of $\boldsymbol{Z}$. The non-normalized composite Kullback–Leibler divergence for a model with density in $\mathcal{F}$ is $d_T(\boldsymbol{\psi}) = \mathrm{E}_o\{-\log L_C(\boldsymbol{\psi}; \mathcal{Z})\}$, where E_o is the expectation under g. The divergence of the model estimated by maximum composite likelihood (with $\hat{\boldsymbol{\psi}}$ as estimated parameter) to the truth is thus

$$d_T(\hat{\boldsymbol{\psi}}) = \mathrm{E}_o\{-\log L_C(\boldsymbol{\psi}; \mathcal{Z})\} \mid_{\boldsymbol{\psi}=\hat{\boldsymbol{\psi}}}, \tag{14}$$

but this is impossible to evaluate unless we know g. Varin and Vidoni (2005) showed that a biased estimator of (14) is $-\log L_C(\hat{\boldsymbol{\psi}}; \mathcal{Z})$, and adjusted for the bias with a first-order correction. Now, suppose that $\hat{\boldsymbol{\psi}}^*$ is a bootstrap replicate of $\hat{\boldsymbol{\psi}}$, and let E^* denote the expectation with respect to the bootstrap distribution of $\hat{\boldsymbol{\psi}}$. With arguments similar to those in Cavanaugh and Shumway (1997), one can show under the usual regularity conditions that

$$\mathrm{Bias}_T^* = -2\left[\mathrm{E}^*\left\{-\log L_C\left(\hat{\boldsymbol{\psi}}^*; \mathcal{Z}\right)\right\} + \log L_C\left(\hat{\boldsymbol{\psi}}; \mathcal{Z}\right)\right] \tag{15}$$

converges almost surely to the bias of $-\log L_C(\hat{\boldsymbol{\psi}}; \mathcal{Z})$ as $T \to \infty$. A Monte Carlo estimator

from B bootstrap replicates yields a strongly consistent estimator of Bias_T^* as $B \to \infty$,

$$\hat{\text{Bias}}_T^\star = -\frac{2}{B}\sum_{b=1}^{B}\left[-\log L_C\left\{\hat{\boldsymbol{\psi}}_b^*; t_{\boldsymbol{\lambda}}(\mathcal{Y})\right\} + \log L_C\left\{\hat{\boldsymbol{\psi}}; t_{\boldsymbol{\lambda}}(\mathcal{Y})\right\}\right]. \tag{16}$$

Thus, a natural estimator of twice the quantity in (14) is

$$-2\log L_C\left\{\hat{\boldsymbol{\psi}}; t_{\boldsymbol{\lambda}}(\mathcal{Y})\right\} - 2\,\hat{\text{Bias}}_T^\star = \frac{1}{B}\sum_{b=1}^{B}\left[2\log L_C\left\{\hat{\boldsymbol{\psi}}; t_{\boldsymbol{\lambda}}(\mathcal{Y})\right\} - 4\log L_C\left\{\hat{\boldsymbol{\psi}}_b^*; t_{\boldsymbol{\lambda}}(\mathcal{Y})\right\}\right]. \tag{17}$$

For T and B large enough, model selection based on CLIC and (17) should be equivalent.

3.4.2 Unknown margins

Suppose that $\boldsymbol{\lambda}$ in $t_{\boldsymbol{\lambda}}$ is estimated by $\hat{\boldsymbol{\lambda}}$, and we are interested in finding the best model for $\mathcal{Z} = t_{\hat{\boldsymbol{\lambda}}}(\mathcal{Y})$ within $\mathcal{F}$. An attractive property of the bootstrap-based estimator of the non-normalized composite Kullback–Leibler divergence developed in Section 3.4.1 is that the effect of estimating the margins can be accounted for. In computing the maximum composite likelihood estimate of $\boldsymbol{\psi}$ for the b-th bootstrap replicate, $b = 1, \ldots, B$, we estimate the marginal parameters from the bootstrapped data, yielding an estimate $\hat{\boldsymbol{\lambda}}_b^*$. We make this explicit by writing the estimates $\hat{\boldsymbol{\psi}}$ and $\hat{\boldsymbol{\psi}}_b^*$ as functions of $\hat{\boldsymbol{\lambda}}$ and $\hat{\boldsymbol{\lambda}}_b^*$, respectively. The expectation $\text{E}^\star$ in (15) with respect to the bootstrap distribution of $\hat{\boldsymbol{\psi}}$ takes the estimation of the margins into account. Following (17), our criterion for model selection is

$$\text{CLIC}^{\text{b}} = \frac{1}{B}\sum_{b=1}^{B}\left[2\log L_C\left\{\hat{\boldsymbol{\psi}}\left(\hat{\boldsymbol{\lambda}}\right); t_{\hat{\boldsymbol{\lambda}}}(\mathcal{Y})\right\} - 4\log L_C\left\{\hat{\boldsymbol{\psi}}_b^*\left(\hat{\boldsymbol{\lambda}}_b^*\right); t_{\hat{\boldsymbol{\lambda}}}(\mathcal{Y})\right\}\right], \tag{18}$$

and the model minimizing this should be chosen. As a full likelihood is a composite likelihood, this could also be used with full likelihood inference.

The matrices $\hat{\text{H}}(\hat{\boldsymbol{\psi}})$ and $\hat{\text{J}}(\hat{\boldsymbol{\psi}})$ required for the calculation of confidence intervals or CLIC are often cumbersome to compute, and careful application of pseudo-inverse procedures may be needed if $\hat{\text{H}}(\hat{\boldsymbol{\psi}})$ is singular, especially for complex models with many parameters. This further supports the use of CLIC^{b}, whose calculation costs the same as a bootstrap.

Expressions asymptotically equivalent to (15) could be used, as in Shibata (1997, Section 2), leading to different but asymptotically equivalent specifications of CLIC^{b}.

3.4.3 Simulation study

We perform two experiments with three procedures: P^{k}, in which the correct margins are used when fitting the models and CLIC is used for selection; P^{u}, in which the marginal distributions are supposed to be GEV and estimated in a first step, then transformed before fitting the dependence models and using CLIC for selection; and P^{b}, which is like P^{u} but uses $\mathrm{CLIC}^{\mathrm{b}}$ in (18) for model selection with a non-parametric block bootstrap ($B = 200$), in which each replicate is a block. In each case the dependence models are fitted using the approach of Section 2.2. The first procedure approximates the best that CLIC can do.

In the first experiment, we generated 40 independent replicates at $D \in \{25, 100, 225\}$ grid points of a Smith field (Smith, 1990) with common standard Fréchet margins and twice the 2×2 identity matrix as covariance matrix, and used P^{k}, P^{u} and P^{b} to choose between an isotropic Smith model labelled SM_0 and a two-parameter Brown–Resnick model labelled BR_1; the latter is over-complex because the Smith field corresponds to the Brown-Resnick field with $\alpha = 2$ (e.g., Huser and Davison, 2013). Table 1 shows that P^{k} correctly chooses SM_0 for any D in around 92% of 200 replications. This figure is much lower for P^{u} and, due to unaccounted variation from the estimation of the margins, drops to as low as 20% when D increases, whereas P^{b} achieves performance close to that of P^{k}.

In a second experiment with a configuration that could be realistic in an environmental application, we generated 40 independent replicates at $D \in \{25, 100, 225\}$ grid points of a Brown–Resnick field with common standard Fréchet margins, $\rho = 2$ and $\alpha = 1$, and used P^{k}, P^{u} and P^{b} to choose between BR_1 and a simpler Brown–Resnick model labelled BR_0 with $\rho = 2$ fixed and α estimated. Table 1 shows that P^{k} correctly chooses BR_0 approximately 84% of the time for any D, as would be expected in the full likelihood setting with n large. The frequency of true selection ranges from 28% and 44% with P^{u}, and is much higher (between 76% and 80%) for P^{b}.

According to the paired proportions test of McNemar (1947), all tests of differences between P^{u} and P^{b} are significant at the 95% level for both experiments (not shown).

	$P^k/P^u/P^b$		
True/Alternative	$D = 25$	$D = 100$	$D = 225$
SM_0/BR_1	93/82/89	90/54/90	94/20/81
BR_0/BR_1	84/44/80	84/30/76	85/28/76

Table 1: Frequency (in %, computed over 200 repetitions) of selection of the true (simpler) model for each experiment, procedure and value of D.

Thus, if the marginal and dependence parameters have to be estimated in two distinct steps and if composite likelihood is used, we strongly advocate the use of $CLIC^b$, (18), rather than CLIC, (13).

In the second experiment, we also compared the 95% confidence intervals of the range parameter estimates of BR_1 calculated using the estimated sandwich covariance matrix and the non-parametric block bootstrap (Davison and Hinkley, 1997, basic intervals in §5.2) with logarithm as variance-stabilizing transform; see Figure 11 for $D \in \{25, 225\}$. The coverages of the sandwich-based intervals drop from 61% to 39% as D increases from 25 to 225, whereas the corresponding values for the bootstrap-based intervals are 90% and 85%, lower than the nominal level but not catastrophically so.

4 Case study

4.1 Max-stability and validation set

We split the region considered into 24 windows of 25–36 grid points each (see Figure 2) and applied the approach outlined in Section 3.3. Figure 2 displays the window-month combinations for which the hypothesis of max-stability was rejected for PROD, and which thus constitute its validation set; similar patterns are obtained for CAPE and SRH (not shown). Around 15% of the window-month combinations failed the max-stability test with level 5% for each variable. Considering larger windows led to a smaller proportion of

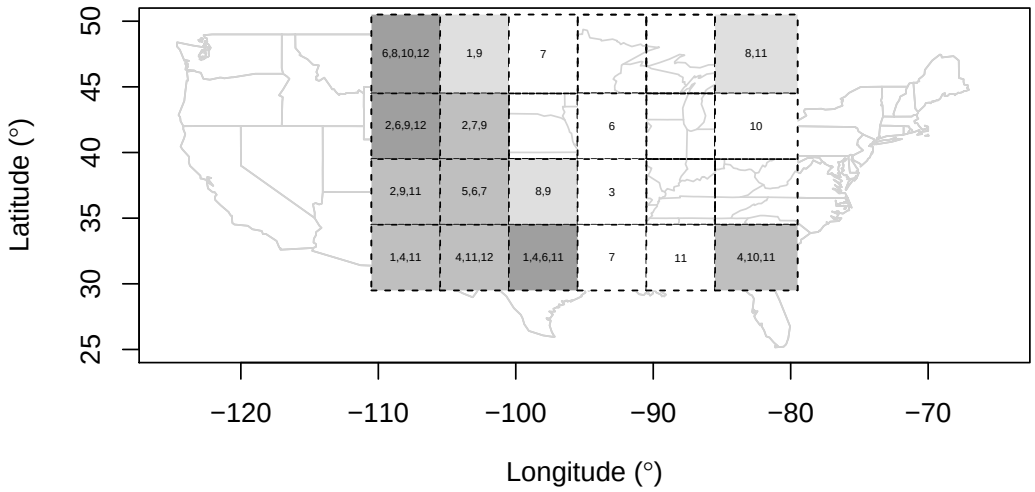


Figure 2: Validation set for PROD. For each window, the numbers indicate the months (1 corresponds to January, ..., 12 to December) constituting the validation dataset. The shading indicates the number of months.

rejections, suggesting that a max-stable model is reasonable.

The windows associated with the largest number of rejections tend to cluster around the western part of the region, suggesting that closeness to max-stability varies across space. It also seems to vary across the year: rejected months often correspond to early winter (e.g., November) for PROD, late summer (e.g., August) for CAPE, and late winter and spring (e.g., February) for SRH.

4.2 Results

We applied the model described in Section 3.1.2 to our data, with $k_1 \in \{2, 3, 4\}$ knots in the ENSO direction and $k_2 \in \{4, 5\}$ knots in the month direction. The knots for ENSO are placed evenly between the 10% and 90% quantiles of its values, i.e., between -1.06°C and 1.16°C, and those for months are positioned evenly between 0.5 and 12.5, both of which represent mid-December and correspond to the same cyclic spline values. We also fitted a

range parameter with no covariates. For each variable, the calibration set corresponds to all corresponding data apart from the validation set. We fitted all models to the calibration set using the truncated pairwise likelihood approach described in Section 2.2 with $c = 2$.

We assessed the uncertainty of our estimates with basic confidence intervals, using non-parametric block bootstrap with 200 replicates. For the range parameter, we used the logarithm as a variance-stabilizing transformation (Davison and Hinkley, 1997, p. 195) and derived the basic confidence intervals for log range before transforming them back to the original scale. For model selection, we used CLIC^{b} in (18) with the same bootstrap replicates. We resampled blocks comprising the 37 years of data from all grid points to retain the spatial structure of the observations. We chose 19 resampling blocks (18 of two consecutive years and one of one year) to preserve some dependence between December and January.

Table 2 shows that the best models for PROD and CAPE have two and four knots in the ENSO and month directions, and that the best for SRH involves two and five knots. These models clearly outperform the one with constant range, suggesting that incorporating ENSO and the month is valuable. Two knots seem enough to capture the ENSO effect visually; compare Figure 3 and those in Section 6.5 of the Supplementary Material. Taking more than two knots also increases the uncertainty on the parameter estimates (not shown). Below, by 'model' we mean the best model for each of SRH, CAPE and PROD.

The estimates of the smoothness parameter α in Table 3 suggest that the models for PROD and CAPE are slightly rougher than that for SRH. The estimates of the parameters in (4) show moderate anisotropy for all three variables, with a non-negligible compression in the longitude direction (r ranges from 0.6 to around 0.8) but only a small rotation κ. A slight systematic downward bias for α was corrected using the bootstrap replicates.

Figure 3 shows that the range parameter ρ is lowest for all variables in July–September and highest in December–May. High ENSO values are associated with higher values of ρ, which occur in late winter and spring (February–May); as a function of ENSO, ρ exhibits a

Knots	**PROD**	**CAPE**	**SRH**
None	19'519'829	18'472'723	16'552'412
2×4	**19′510′372**	**18′466′193**	16'516'130
3×4	19'515'502	18'468'421	16'629'860
4×4	19'520'216	18'472'426	16'520'391
2×5	19'511'256	18'466'535	**16′516′015**
3×5	19'519'077	18'470'945	16'521'017
4×5	19'527'238	18'475'342	16'525'644

Table 2: Values of CLIC^{b} for different configurations of $k_1 \times k_2$, where k_1 and k_2 are the number of knots in the ENSO and month direction, respectively.

Parameter	**PROD**		**CAPE**		**SRH**	
α	1.29	$(1.27, 1.31)$	1.33	$(1.30, 1.36)$	1.47	$(1.44, 1.50)$
r	0.72	$(0.71, 0.73)$	0.76	$(0.75, 0.78)$	0.61	$(0.60, 0.62)$
κ	-0.08	$(-0.10, -0.06)$	-0.13	$(-0.15, -0.10)$	-0.07	$(-0.08, -0.05)$

Table 3: For each variable, estimates of the model parameters (an asterisk indicates that the estimate has been bootstrap bias-corrected) with their 90% bootstrap confidence intervals in brackets.

kink at 0°C for each month and increases above that value. Some of the patterns for PROD and CAPE are less clear and further data would be needed to determine them better.

For any value of ENSO and each month, we can compute the bivariate extremal coefficient of our model by combining (7) and (12). Figure 4 shows parameter estimates obtained from 200 bootstrap replicates for grid points that are 1° longitude apart. For ENSO = 0°C, the estimates are rather stable across months, though they are higher in June–August for SRH. The seasonal variation is more pronounced when ENSO = −1°C and ENSO = 1°C, especially for SRH, for which the estimated extremal coefficient during an El Niño event in July is appreciably higher than in November–April. There is a clear decrease of the extremal coefficient (related to an increase of the range parameter) in late

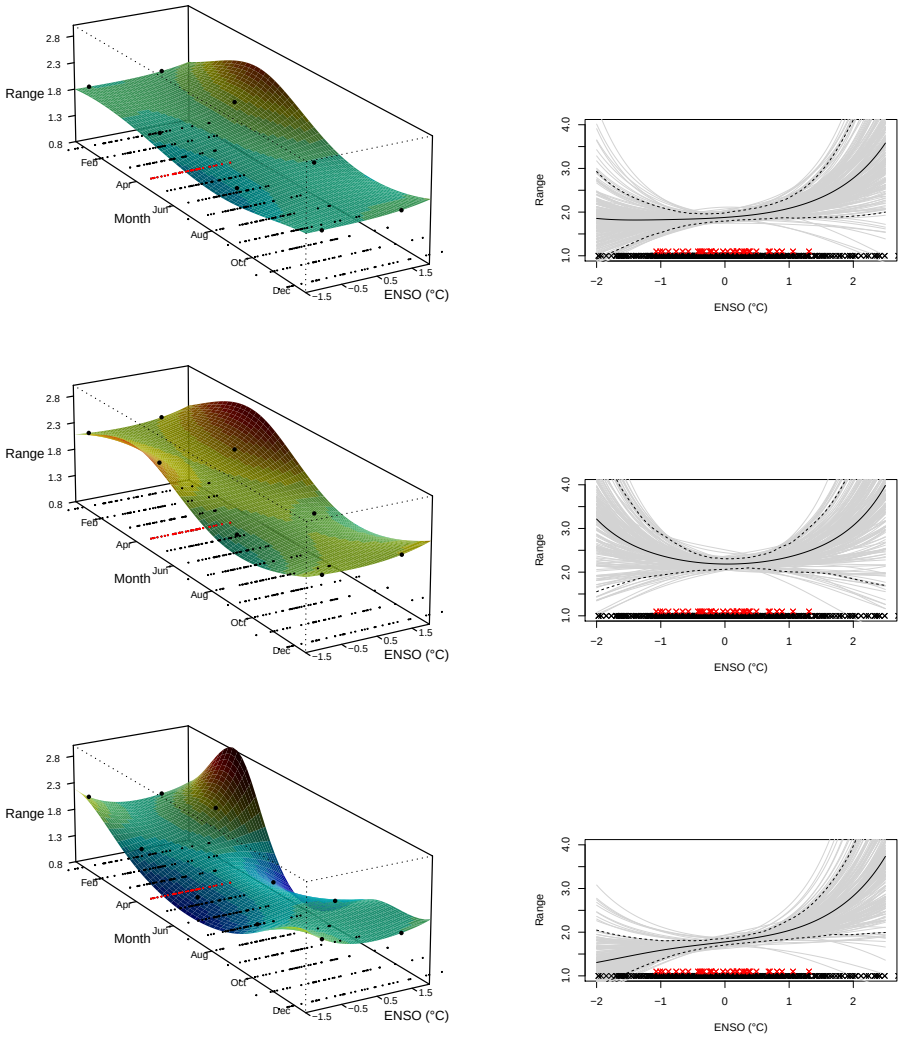


Figure 3: Trend surfaces for the estimated range parameter $\hat{\rho}$ of the model for PROD (top), CAPE (middle) and SRH (bottom). The right-hand panels show slices of the surface in April (black) with the values of $\exp\{2\log(\hat{\rho}) - \log(\hat{\rho}_b^\star)\}$ $(b = 1, \ldots, 200)$ (grey), where $\hat{\rho}_b^\star$ is the b-th bootstrap estimate, and the 90% bootstrap pointwise confidence limits (dashed). On all plots, the rug represents the ENSO values for April (red) and other months (black). The larger black dots in the left-hand panels indicate the knots.

winter and spring during El Niño years. For SRH, Figure 5 displays the value of the estimated model bivariate extremal coefficient between each point and a reference point at the center of the map. The extremal coefficients are lower in April than in August for the three chosen values of ENSO (−1°C, 0°C, 1°C) and decrease with ENSO in April; this indicates increased extremal dependence, consistent with the larger range parameter. The contours

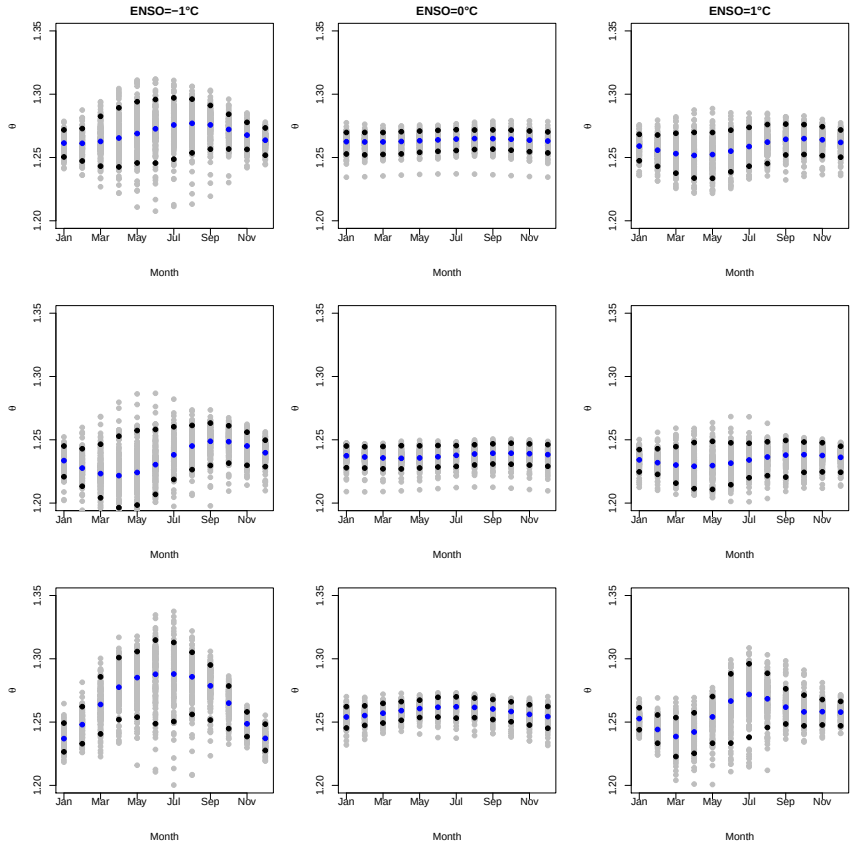


Figure 4: Bias-corrected estimates (blue) of the modeled bivariate extremal coefficient for PROD (top), CAPE (middle) and SRH (bottom), when ENSO equals -1°C (left), 0°C (center) and 1°C (right), for two grid points 1° longitude apart. The grey dots are the 200 values of $h^{-1}\{2h(\hat{\theta}) - h(\hat{\theta}_b^\star)\}$, $b = 1, \ldots, 200$, where $\hat{\theta}_b^\star$ is the b-th bootstrap estimate and $h(x) = \log\{(x-1)/(2-x)\}$, for $x \in [1, 2]$. The black dots indicate the lower and upper 90% bootstrap pointwise confidence limits.

in Figure 5 nicely illustrate the variation with ENSO of the spatial extent of the extreme events of SRH.

4.3 Model validation

We assessed our model's performance on the validation set specified in Section 4.1. Figure 6 shows that the theoretical pairwise extremal coefficients computed from our model agree with the empirical ones, despite slight underestimation in the right panel. For PROD and SRH in the chosen window-month combinations, higher values of ENSO are associated with lower empirical extremal coefficients than when ENSO ≈ 0°C, which is not the case

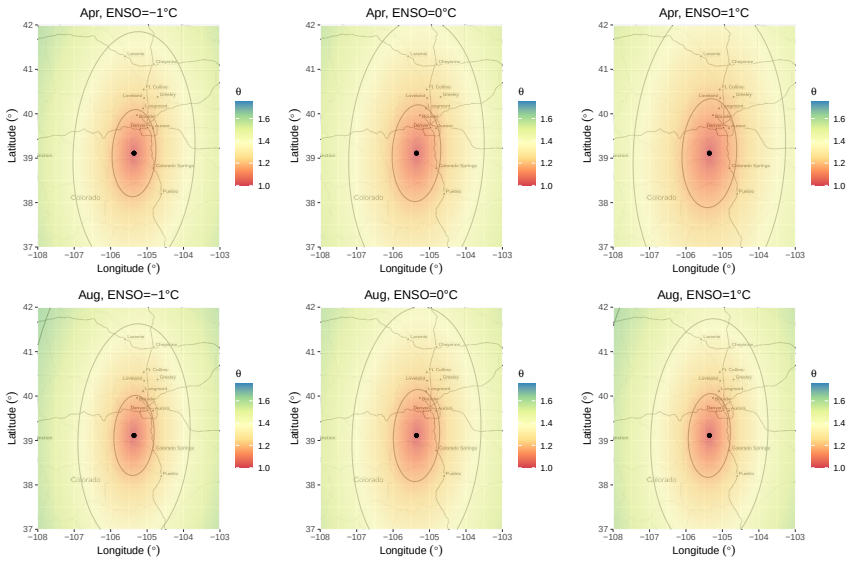


Figure 5: Bias-corrected estimates of the model's bivariate extremal coefficient for SRH (with one reference fixed in Colorado, indicated by the black dots) when ENSO equals $-1°$C (left), $0°$C (center) and $1°$C (right), in April (top) and August (bottom). The grey contour lines represent the 1.2, 1.4 and 1.6 levels.

for CAPE in the chosen window in August; our model captures these effects well, and has satisfactory overall out-sample performance.

The few departures between our model and the data probably stem from the spatially-constant extremal dependence in our model and the heterogeneity of the region in terms of weather influences, reflected by the spatially-varying suitability of max-stability, as seen in Section 4.1. Koch et al. (2021, Figure 8) showed that the February maxima at each grid point increase significantly with ENSO around the Gulf of Mexico, but decrease significantly with ENSO over the rest of the region. The marginal impact of ENSO varies across space, and its effects on the dependence may vary over space. The fact that the models' extremal coefficient is computed for particular values of distance and ENSO, whereas the boxplots of Figure 6 are built using a range of distances and ENSO values, may also contribute to the departures.

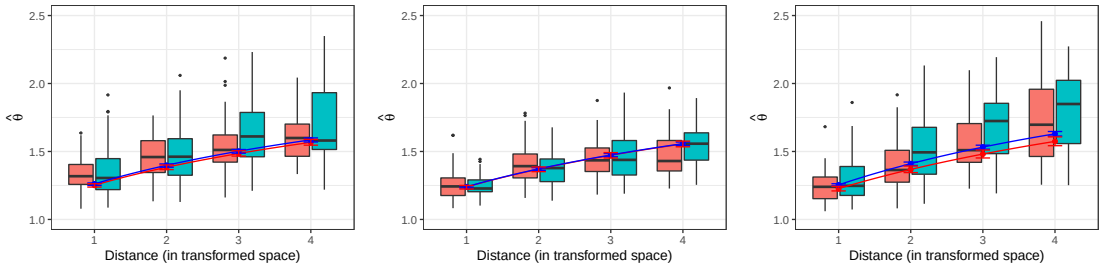


Figure 6: Out-sample performance of the models for PROD (left), CAPE (center) and SRH (right) for the window-month combinations (8-February), (17-August) and (2-March), respectively, where the windows are numbered from West to East and North to South. The lines depict the modeled extremal coefficients computed at ENSO=1°C (red) and 0°C (blue) with respect to distance in the transformed space, computed using (4) with the estimated κ and r. The whiskers indicate pointwise basic bootstrap 90% confidence limits. The four pairs of boxplots summarize the empirical estimates of the extremal coefficient for pairs of grid points whose distance in the transformed space lies in the ranges $[0.5, 1.5)$, $[1.5, 2.5)$, $[2.5, 3.5)$ and $[3.5, 4.5)$. The red and blue boxes correspond to ENSO> 0.5°C and $|$ENSO$| < 0.2$°C, respectively.

4.4 Meteorological explanation

As mentioned in Section 2.1, the range parameter ρ in (3) can be interpreted as a characteristic spatial dimension of individual extreme events, so might be viewed as a characteristic dimension of cyclones or thunderstorms systems (including multi-cell storms, squall lines, supercells and mesoscale convective systems). Thus our results suggest that cyclones and thunderstorm systems are more localized in summer than in winter, in line with the fact that winter weather systems are generally larger. Our results also suggest that such systems are larger during El Niño events than during neutral ENSO states or La Niña events. Koch et al. (2021) found that, in late winter and spring, the maxima of PROD, CAPE and SRH tend to be larger during La Niña years, perhaps leading to more intense thunderstorm systems. The combination of both findings points to more spatially widespread but less intense thunderstorm systems during El Niño years than La Niña years. El Niño winter events tend to be associated with positive and negative temperature anomalies in respectively the northern and southern part of the US (e.g., Ropelewski and Halpert, 1986; Zhang et al., 2011), and thus with a less pronounced north-south temperature gradient than during neutral ENSO

states or La Niña episodes. El Niño periods are also linked to positive rainfall anomalies in the southern part of the US and especially California (e.g., Ropelewski and Halpert, 1986; Jong et al., 2016). These anomalies tend to persist during the following spring, while progressively weakening (see https://www.oc.nps.edu/webmodules/ENSO/NA_EN.html). The temperature gradient is a key factor of instability, as the shock between warm and cold air typically triggers rising motion, and larger gradients can be expected to be linked with more localized and more dynamic cyclones or mesoscale convective systems. Another, less plausible, explanation is that the combination of the warming in the northern part of the US and increased rainfall in the south associated with El Niño leads to larger areas of instability, of which warm air and moisture are two important ingredients.

The main drivers of weather vary across our region, so finding an over-arching interpretation of the statistical findings is delicate. More investigations would be needed to further shed light on the very complex physical mechanisms involved. The link between ENSO and the spatial extent of weather phenomena has received relatively little attention from researchers; see, e.g., Lyon (2004) and Lyon and Barnston (2005) in the case of the droughts and rainfall extremes.

5 Discussion

In this paper we use space-time max-stable models whose dependence structure involves covariates such as large-scale atmospheric signals to capture the temporal non-stationarity of the extremal spatial dependence of the variables PROD, CAPE and SRH associated with severe US thunderstorms. We use a fractional Brown–Resnick field whose range parameter depends on ENSO and month through a tensor product spline to shed light on how thse variables affect the spatial extents of these phenomena.

One novel methodological contribution is a max-stability test, based on empirical likelihood and the bootstrap, that accounts for unknown margins. This provides an additional diagnostic to assess whether a sub-asymptotic model should replace a max-stable model.

Another is a hypothesis-testing-based method to constitute the validation set, which enables a stringent assessment of out-sample performance, and we tailor this to the case study using our max-stability test. A third, a bootstrap-based estimator of the composite Kullback–Leibler divergence, enables better model selection than does the use of CLIC, especially when one first estimates marginal distributions and then uses composite likelihood separately to estimate a dependence structure.

Max-stability appears to be an appropriate assumption for our data. For each of PROD, CAPE and SRH, the range parameter ρ is lowest from July to September and highest from December to May. Higher ENSO values are associated with a shift of the latter period to February–May and with higher ρ, which implies that extreme events are more spatially extended during El Niño events. The uncertainty about this result is larger for PROD and CAPE than for SRH. Our findings, combined with those of Koch et al. (2021), suggest that thunderstorm systems during El Niño events may be less intense but larger in scale than during neutral ENSO states or La Niña events.

Our model accounts for variation of extremal dependence across time but not over space, a drawback for regions with heterogeneous weather influences. Refining it to allow spatial variation in the dependence structure would be useful, though a simpler option would be to apply the model separately to sub-regions; this would enable a more detailed understanding of the ENSO effect. This approach, and studying the effects of other atmospheric signals, such as the North Atlantic Oscillation and the Madden–Julian Oscillation, would also require sufficient data.

Using our model for risk assessment or forecasting would require simulated vectors of covariates $\boldsymbol{x}_t$ $(t = 1, \ldots, T)$, entailing treating them as realizations of random vectors $\boldsymbol{X}_t$. Point 2 in the definition of our general model in Section 3.1.1 would then be: the spatial fields $\{Z(\boldsymbol{s}, 1) : \boldsymbol{s} \in \mathcal{X}\}, \ldots, \{Z(\boldsymbol{s}, T) : \boldsymbol{s} \in \mathcal{X}\}$ are independent conditionally on $\boldsymbol{X}_1, \ldots, \boldsymbol{X}_T$. Unconditionally, any temporal dependence would be driven by the dynamics of the random process $\{\boldsymbol{X}_t : t = 1, \ldots, T\}$, but without specific assumptions on that

dynamics, the resulting space-time model $\{Z(\boldsymbol{s}, t) : \boldsymbol{s} \in \mathcal{X}, t = 1, \ldots, T\}$ will not be a space-time max-stable field, unlike models developed by Davis et al. (2013), Huser and Davison (2014) or Embrechts et al. (2016).

References

Allen, J. T. and Tippett, M. K. (2015), 'The characteristics of United States hail reports: 1955-2014', *Electronic Journal of Severe Storms Meteorology* **10**(3), 1–31.

Allen, J. T., Tippett, M. K. and Sobel, A. H. (2015), 'Influence of the El Niño/Southern Oscillation on tornado and hail frequency in the United States', *Nature Geoscience* **8**, 278–283.

Bacro, J.-N., Bel, L. and Lantuéjoul, C. (2010), 'Testing the independence of maxima: from bivariate vectors to spatial extreme fields', *Extremes* **13**(2), 155–175.

Blanchet, J. and Davison, A. C. (2011), 'Spatial modeling of extreme snow depth', *The Annals of Applied Statistics* **5**(3), 1699–1725.

Brooks, H. E. (2013), 'Severe thunderstorms and climate change', *Atmospheric Research* **123**, 129–138.

Brooks, H. E., Lee, J. W. and Craven, J. P. (2003), 'The spatial distribution of severe thunderstorm and tornado environments from global reanalysis data', *Atmospheric Research* **67–68**, 73–94.

Brown, B. M. and Resnick, S. I. (1977), 'Extreme values of independent stochastic processes', *Journal of Applied Probability* **14**(4), 732–739.

Buhl, S. and Klüppelberg, C. (2016), 'Anisotropic Brown–Resnick space-time processes: estimation and model assessment', *Extremes* **19**(4), 627–660.

Castruccio, S., Huser, R. and Genton, M. G. (2016), 'High-order composite likelihood inference for max-stable distributions and processes', *Journal of Computational and Graphical Statistics* **25**(4), 1212–1229.

Cavanaugh, J. E. and Shumway, R. H. (1997), 'A bootstrap variant of AIC for state-space model selection', *Statistica Sinica* **7**(2), 473–496.

Coles, S. (2001), *An Introduction to Statistical Modeling of Extreme Values*, Springer-Verlag London.

Cooley, D., Naveau, P. and Poncet, P. (2006), Variograms for spatial max-stable random fields, *in* P. Bertail, P. Soulier and P. Doukhan, eds, 'Dependence in Probability and Statistics', Springer, New York, pp. 373–390.

Davis, R. A., Klüppelberg, C. and Steinkohl, C. (2013), 'Max-stable processes for modeling extremes observed in space and time', *Journal of the Korean Statistical Society* **42**(3), 399–414.

Davison, A. C. and Hinkley, D. V. (1997), *Bootstrap Methods and their Application*, Cambridge Series in Statistical and Probabilistic Mathematics, Cambridge University Press.

Davison, A. C., Huser, R. and Thibaud, E. (2013), 'Geostatistics of dependent and asymptotically independent extremes', *Mathematical Geosciences* **45**(5), 511–529.

Davison, A. C., Huser, R. and Thibaud, E. (2018), Spatial extremes, *in* A. E. Gelfand, M. Fuentes, J. A. Hoeting and R. L. Smith., eds, 'Handbook of Environmental and Ecological Statistics', CRC Press.

Davison, A. C., Padoan, S. A. and Ribatet, M. (2012), 'Statistical modeling of spatial extremes', *Statistical Science* **27**(2), 161–186.

de Carvalho, M. and Ramos, A. (2012), 'Bivariate extreme statistics, II', *Revstat-Statistical Journal* **10**, 81–104.

de Haan, L. (1984), 'A spectral representation for max-stable processes', *The Annals of Probability* **12**(4), 1194–1204.

de Haan, L. and Ferreira, A. (2006), *Extreme Value Theory: An Introduction*, Springer-Verlag New York.

Dombry, C., Engelke, S. and Oesting, M. (2016), 'Exact simulation of max-stable processes', *Biometrika* **103**(2), 303–317.

Dombry, C., Ribatet, M. and Stoev, S. (2018), 'Probabilities of concurrent extremes', *Journal of the American Statistical Association* **113**(524), 1565–1582.

Doswell III, C. A. (2015), Mesoscale meteorology — severe storms, *in* 'Encyclopedia of Atmospheric Sciences', pp. 361–368.

Edwards, R., Allen, J. T. and Carbin, G. W. (2018), 'Reliability and climatological impacts of convective wind estimations', *Journal of Applied Meteorology and Climatology* **57**(8), 1825–1845.

Einmahl, J. H. J. and Segers, J. (2009), 'Maximum empirical likelihood estimation of the spectral measure of an extreme-value distribution', *The Annals of Statistics* **37**(5B), 2953–2989.

Embrechts, P., Koch, E. and Robert, C. Y. (2016), 'Space–time max-stable models with spectral separability', *Advances in Applied Probability* **48**(A), 77–97.

Gabda, D., Towe, R., Wadsworth, J. and Tawn, J. (2012), 'Discussion of "Statistical Modelling of Spatial Extremes" by A.C. Davison, S.A. Padoan and M. Ribatet', *Statistical Science* **27**(2), 189–192.

Gilleland, E., Brown, B. G. and Ammann, C. M. (2013), 'Spatial extreme value analysis to project extremes of large-scale indicators for severe weather', *Environmetrics* **24**(6), 418–432.

Heaton, M. J., Katzfuss, M., Ramachandar, S., Pedings, K., Gilleland, E., Mannshardt-Shamseldin, E. and Smith, R. L. (2011), 'Spatio-temporal models for large-scale indicators of extreme weather', *Environmetrics* **22**(3), 294–303.

Heffernan, J. E. and Tawn, J. A. (2004), 'A conditional approach for multivariate extreme values (with discussion)', *Journal of the Royal Statistical Society: Series B (Statistical Methodology)* **66**(3), 497–546.

Hoerling, M. P., Kumar, A. and Zhong, M. (1997), 'El Niño, La Niña, and the nonlinearity of their teleconnections', *Journal of Climate* **10**(8), 1769–1786.

Huser, R. and Davison, A. C. (2013), 'Composite likelihood estimation for the Brown–Resnick process', *Biometrika* **100**(2), 511–518.

Huser, R. and Davison, A. C. (2014), 'Space-time modelling of extreme events', *Journal of the Royal Statistical Society: Series B (Statistical Methodology)* **76**(2), 439–461.

Huser, R. and Genton, M. G. (2016), 'Non-stationary dependence structures for spatial extremes', *Journal of Agricultural, Biological, and Environmental Statistics* **21**(3), 470–491.

Huser, R., Opitz, T. and Thibaud, E. (2021), 'Max-infinitely divisible models and inference for spatial extremes', *Scandinavian Journal of Statistics* **48**(1), 321–348.

Huser, R. and Wadsworth, J. L. (2019), 'Modeling spatial processes with unknown extremal dependence class', *Journal of the American Statistical Association* **114**(525), 434–444.

Jong, B.-T., Ting, M. and Seager, R. (2016), 'El Niño's impact on California precipitation: Seasonality, regionality, and El Niño intensity', *Environmental Research Letters* **11**(5), 054021.

Kabluchko, Z. and Schlather, M. (2010), 'Ergodic properties of max-infinitely divisible processes', *Stochastic Processes and their Applications* **120**(3), 281–295.

Kabluchko, Z., Schlather, M. and de Haan, L. (2009), 'Stationary max-stable fields associated to negative definite functions', *The Annals of Probability* **37**(5), 2042–2065.

Koch, E., Koh, J., Davison, A. C., Lepore, C. and Tippett, M. K. (2021), 'Trends in the extremes of environments associated with severe U.S. thunderstorms', *Journal of Climate* **34**(4), 1259–1272.

Lepore, C., Tippett, M. K. and Allen, J. T. (2017), 'ENSO-based probabilistic forecasts of March–May US tornado and hail activity', *Geophysical Research Letters* **44**(17), 9093–9101.

Lyon, B. (2004), 'The strength of El Niño and the spatial extent of tropical drought', *Geophysical Research Letters* **31**(21).

Lyon, B. and Barnston, A. G. (2005), 'ENSO and the spatial extent of interannual precipitation extremes in tropical land areas', *Journal of Climate* **18**(23), 5095–5109.

Mannshardt, E. and Gilleland, E. (2013), 'Extremes of severe storm environments under a changing climate', *American Journal of Climate Change* **2**(3A), 47–61.

McNemar, Q. (1947), 'Note on the sampling error of the difference between correlated proportions or percentages', *Psychometrika* **12**(2), 153–157.

Mhalla, L., Chavez-Demoulin, V. and Naveau, P. (2017), 'Non-linear models for extremal dependence', *Journal of Multivariate Analysis* **159**, 49–66.

Opitz, T. (2013), 'Extremal t processes: elliptical domain of attraction and a spectral representation', *Journal of Multivariate Analysis* **122**, 409–413.

Owen, A. B. (2001), *Empirical Likelihood*, Chapman and Hall CRC, New York.

Padoan, S. A., Ribatet, M. and Sisson, S. A. (2010), 'Likelihood-based inference for max-stable processes', *Journal of the American Statistical Association* **105**(489), 263–277.

Pickands, J. (1981), 'Multivariate extreme value distributions', *Bulletin of the International Statistical Institute: Proceedings of the 43rd Session of the International Statistical Institute, Vol. 2 (Buenos Aires)* pp. 859–878, 894–902.

Ropelewski, C. F. and Halpert, M. S. (1986), 'North American precipitation and temperature patterns associated with the El Niño/Southern Oscillation (ENSO)', *Monthly Weather Review* **114**(12), 2352–2362.

Sang, H. and Genton, M. G. (2014), 'Tapered composite likelihood for spatial max-stable models', *Spatial Statistics* **8**, 86–103.

Schlather, M. (2002), 'Models for stationary max-stable random fields', *Extremes* **5**(1), 33–44.

Schlather, M. and Tawn, J. A. (2003), 'A dependence measure for multivariate and spatial extreme values: properties and inference', *Biometrika* **90**(1), 139–156.

Shibata, R. (1997), 'Bootstrap estimate of Kullback-Leibler information for model selection', *Statistica Sinica* **7**, 375–394.

Smith, E. L. and Stephenson, A. G. (2009), 'An extended Gaussian max-stable process model for spatial extremes', *Journal of Statistical Planning and Inference* **139**(4), 1266–1275.

Smith, R. (1990), 'Max-stable processes and spatial extremes', *Unpublished manuscript* .

Tippett, M. K., Lepore, C. and Cohen, J. E. (2016), 'More tornadoes in the most extreme U.S. tornado outbreaks', *Science* **354**(6318), 1419–1423.

Trapp, R. J., Tessendorf, S. A., Godfrey, E. S. and Brooks, H. E. (2005), 'Tornadoes from squall lines and bow echoes. Part I: climatological distribution', *Weather and Forecasting* **20**(1), 23–34.

Varin, C., Reid, N. and Firth, D. (2011), 'An overview of composite likelihood methods', *Statistica Sinica* **21**(1), 5–42.

Varin, C. and Vidoni, P. (2005), 'A note on composite likelihood inference and model selection', *Biometrika* **92**(3), 519–528.

Verbout, S. M., Brooks, H. E., Leslie, L. M. and Schultz, D. M. (2006), 'Evolution of the U.S. tornado database: 1954–2003', *Weather and Forecasting* **21**(1), 86–93.

Zhang, T., Hoerling, M. P., Perlwitz, J., Sun, D.-Z. and Murray, D. (2011), 'Physics of US surface temperature response to ENSO', *Journal of Climate* **24**(18), 4874–4887.

6 Supplement

6.1 For Section 2.2

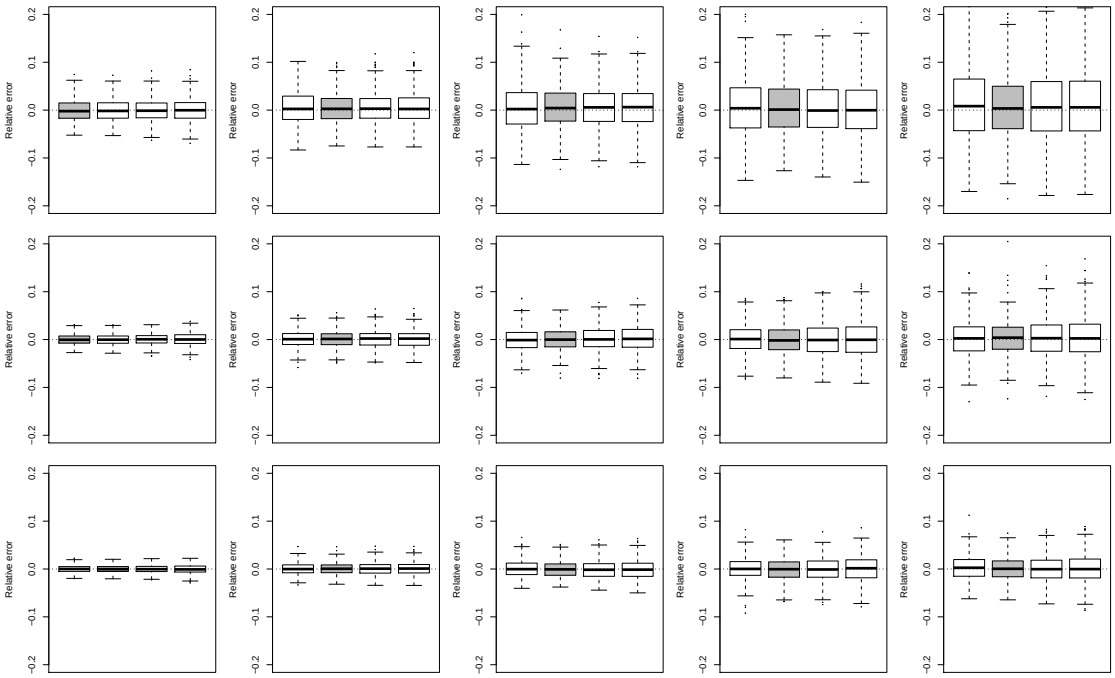


Figure 7: Boxplots of the relative errors of the estimates of ρ for $c = 1, 2, 3, 4$ (from left to right). The boxplot associated with the lowest relative root mean squared error is highlighted in grey. The rows correspond to $D = 25$ (top), 100 (middle), 225 (bottom) and each column corresponds to a value of ρ: $1, 2, 4, 8, 12$ (from left to right).

6.2 For Section 3.1.2

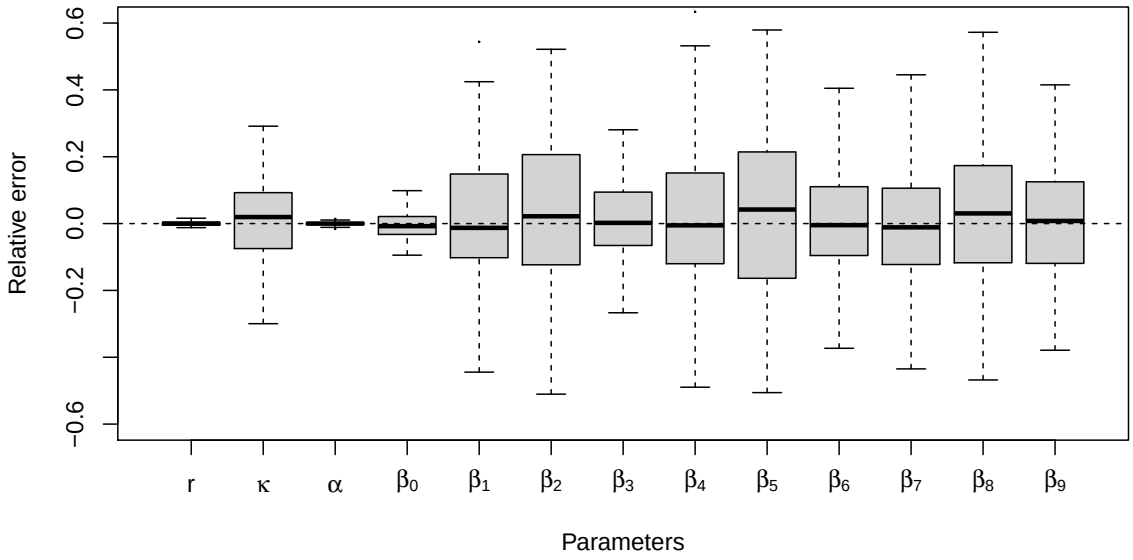


Figure 8: Relative error for the parameters in the simulation study.

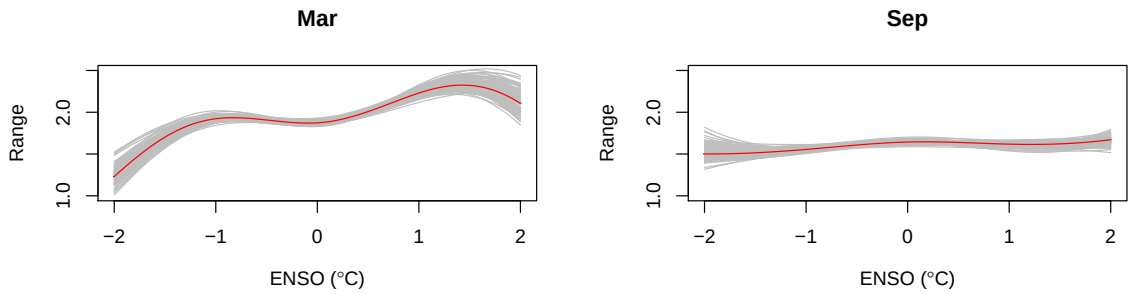


Figure 9: The estimated range parameter with form given in (10), based on the same simulation study as that in Figure 8, for t mod 12 = 3 (March, left) and t mod 12 = 9 (September, right).

6.3 For Section 3.2

6.3.1 Algorithms

Let $\boldsymbol{y}_j = (y_{1,j}, \ldots, y_{D,j})'$ denote the j-th three-hourly observation, empirically transformed to be standard Fréchet-distributed, where D is the number of grid points. Given n three-hourly observations, let $(\boldsymbol{y}_1, \ldots, \boldsymbol{y}_n)' \in \mathbb{R}^{n \times D}$ denote the transformed dataset. The procedure for generating the max-stable vector is

1. Compute $\tilde{R}_j = ||y_{1,j}, \ldots, y_{D,j}||_1$, known as the radial coordinates, where $||\cdot||_1$ is the L_1 norm. Then calculate $\tilde{\boldsymbol{W}}_{\boldsymbol{j}} = \boldsymbol{y}_j / \tilde{R}_j$, $j = 1, \ldots, n$, commonly called the angular coordinates. Keep those $\tilde{\boldsymbol{W}}_j$ for which $\tilde{R}_j > r_0$, with r_0 fixed to be the empirical p-quantile of $\tilde{R}_1, \ldots, \tilde{R}_n$, so the number of observations retained is $n_0 = (1-p)n$, where $0 < p < 1$. Let R_i and $\boldsymbol{W}_i$ $(i = 1, \ldots, n_0)$ denote the coordinates retained.

2. Following the empirical likelihood approach of Einmahl and Segers (2009), but extended to $D > 2$, we find the estimated angular probability measure

$$\hat{Q}(\boldsymbol{w}) = \sum_{i=1}^{n_0} q_i \mathbb{I}_{\{\boldsymbol{W}_i < \boldsymbol{w}\}}, \quad \boldsymbol{w} \in [0,1]^D,$$

   where $\mathbb{I}_{\{\cdot\}}$ is the indicator function and the tilting probabilities $\{q_i\}_{i=1}^{n_0}$ satisfy

$$q_i = \arg\max_{q_i} \prod_{i=1}^{n_0} q_i, \text{ such that } \sum_{i=1}^{n_0} q_i = 1 \text{ and } \sum_{i}^{n_0} q_i \boldsymbol{W}_i / R_i = \boldsymbol{D}^{-1}, \tag{19}$$

   where $\boldsymbol{D}^{-1} = (1/D, \ldots, 1/D)'$, and (19) is solved using Lagrange multipliers.

3. With $\{q_i\}_{i=1}^{n_0}$ and $\{\boldsymbol{W}_i\}_{i=1}^{n_0}$, generate a simple max-stable vector using Algorithm 1, based on Dombry et al. (2016).

Algorithm 1: Simulate max-stable vector using tilting weights

Input: Tilting weights $\{q_i\}_{i=1}^{n_0}$ and vectors $\{\boldsymbol{W}_i\}_{i=1}^{n_0}$

Output: Max-stable D-dimensional vector with standard Frechét margins

Generate $E^\star \sim \text{Exp}(1)$;

Set $R^\star = D/E^\star$;

Set $\boldsymbol{Z} = (Z_1, \ldots, Z_D) = (0, \ldots, 0)$;

while $R^\star > \min\{Z_1, \ldots, Z_D\}$ **do**

  Draw $\boldsymbol{W}' = (W_1', \ldots, W_D')$ from the set $\{\boldsymbol{W}_1, \ldots, \boldsymbol{W}_{n_0}\}$ with sampling probabilities $\{q_1, \ldots, q_{n_0}\}$;

  for $j \leftarrow 1$ **to** D **do**

    Set $Z_j = \max(Z_j, R^\star W_j')$;

  end

  Generate $E^\star \sim \text{Exp}(1)$;

  Set $R^\star = \frac{1}{(1/R^\star + E^\star/D)}$;

end

return $\boldsymbol{Z}$;

6.3.2 Figures and tables

	5%	20%	p-val AD	p-val KS
Max-stable logistic, $\lambda = 0.1$	5.20	20.90	0.77	0.94
Max-stable logistic, $\lambda = 0.5$	4.70	20.30	0.17	0.29
Max-stable logistic, $\lambda = 0.9$	6.12	22.20	0.08	0.20
Normal, $\zeta = 0.1$	5.20	20.20	0.02	0.04
Normal, $\zeta = 0.5$	9.30	26.30	0.00	0.00
Normal, $\zeta = 0.9$	16.20	34.50	0.00	0.00
Normal, $\zeta = 0.99$	7.02	24.02	0.01	0.03

Table 4: Empirical size (%) (top three) and power (%) (bottom three) for tests at the 5% and 20% nominal level with $(B, p) = (200, 0.9)$, for 1000 samples of size $n = 240 \times 40$, and different levels of dependence. The last two columns show the p-values for the Anderson–Darling and Kolmogorov–Smirnoff tests of uniformity for the 1000 p-values.

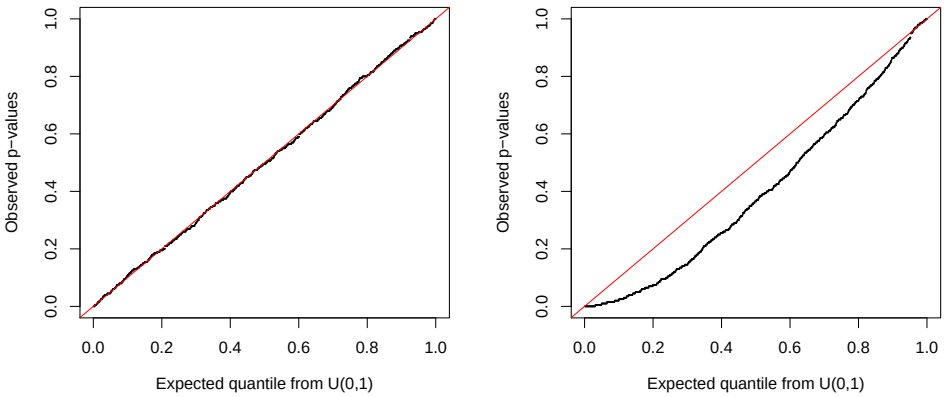


Figure 10: Quantile-quantile plots for the 1000 p-values with the simulation setting involving the max-stable logistic, $\lambda = 0.1$ (left), and normal, $\rho = 0.9$ (right), distributions.

6.4 For Section 3.4

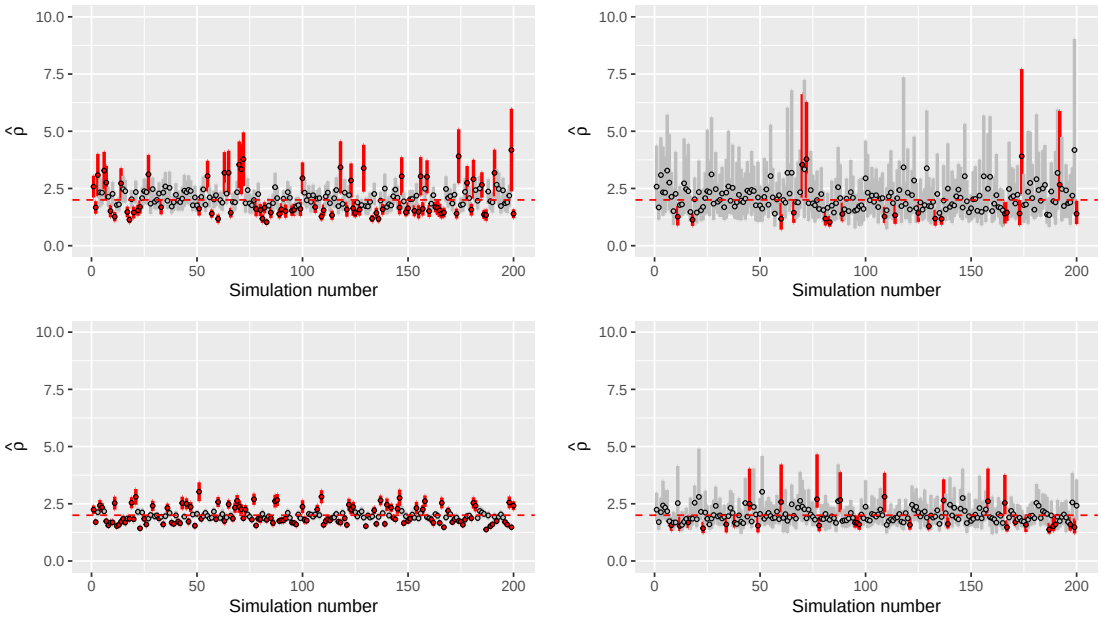


Figure 11: Nominal 95% sandwich (left) and bootstrap (right) confidence intervals for the range parameter ρ (with logarithm as variance stabilizing transform) in the model BR_1 using the two-step estimation procedure, from 200 simulations with 40 replications, $D = 25$ (top) and $D = 225$ (bottom). The red confidence intervals represent those that do not cover the true value represented by the red dashed line.

6.5 For Section 4.2

Figures 12, 13 and 14 show the same plots as the left panels of Figure 3, for the fitted models from Table 2.

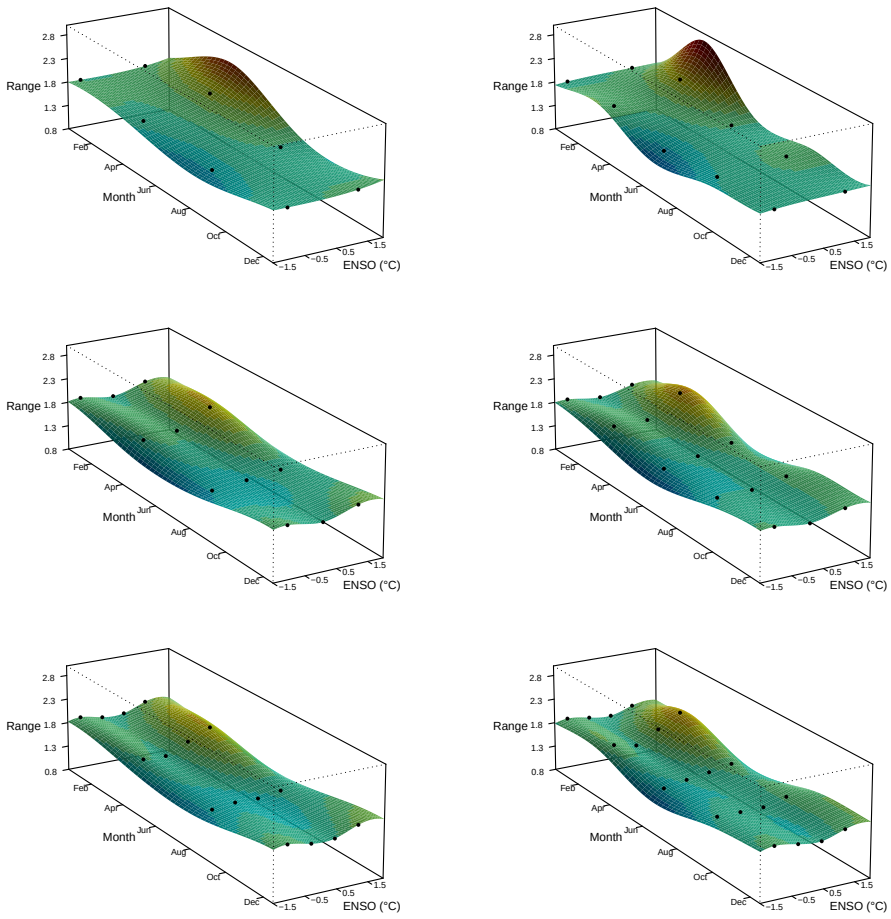


Figure 12: Trend surface plots of the range parameter in the models with (from top left to bottom right) 2×4 , 3×4, 4×4, 2×5, 3×5, 4×5 knots in the ENSO and month direction for PROD. The black dots on the trend surfaces indicate the knots' positions.

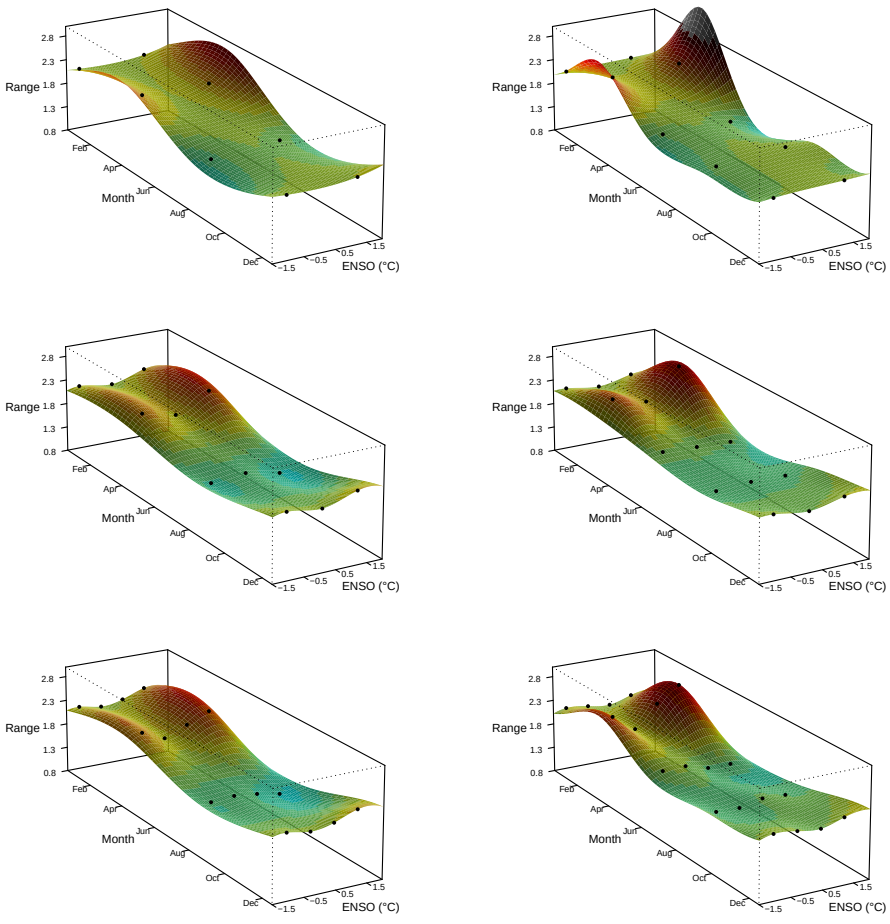


Figure 13: Same as Figure 12, but for CAPE.

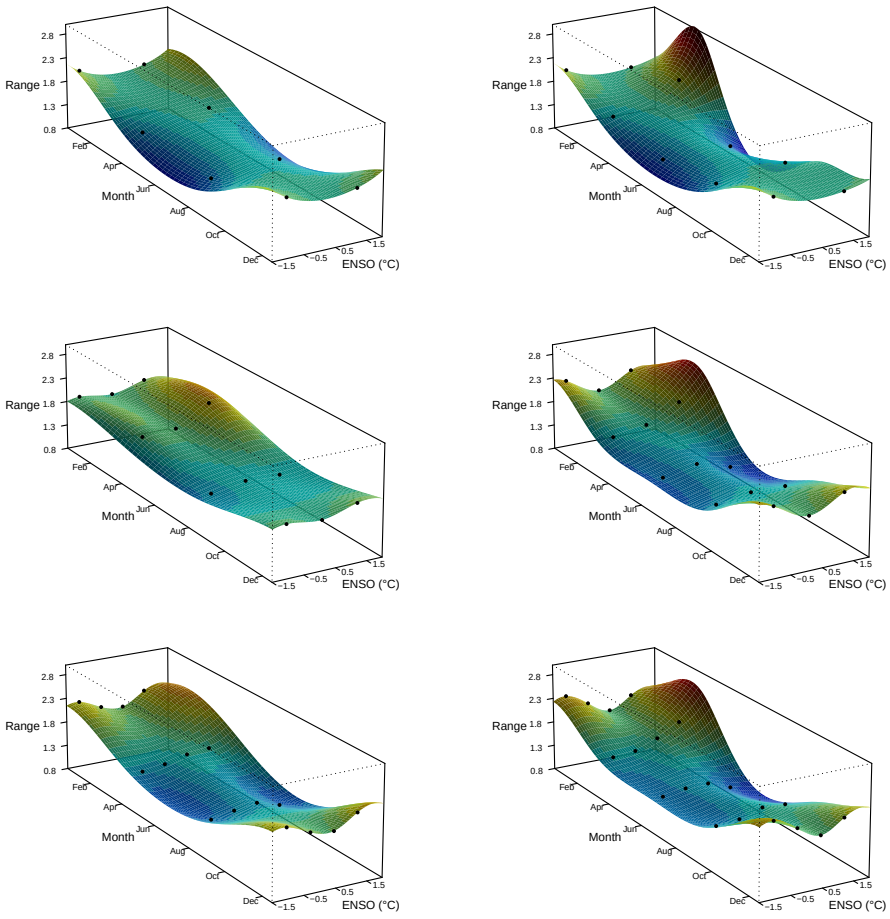


Figure 14: Same as Figure 12, but for SRH.